

Neutrino Telescopes as QCD Microscopes

Valerio Bertone,^a Rhorry Gauld,^b and Juan Rojo^a

^a*Department of Physics and Astronomy, VU University, NL-1081 HV Amsterdam,
and Nikhef Theory Group, Science Park 105, 1098 XG Amsterdam, The Netherlands*

^b*Institute for Theoretical Physics, ETH, CH-8093 Zürich, Switzerland*

E-mail: v.bertone@vu.nl, rgauld@phys.ethz.ch, j.rojo@vu.nl

ABSTRACT: We present state-of-the-art predictions for the ultra-high energy (UHE) neutrino-nucleus cross-sections in charged- and neutral-current scattering. The calculation is performed in the framework of collinear factorisation at NNLO, extended to include the resummation of small- x BFKL effects. Further improvements are made by accounting for the free-nucleon PDF constraints provided by D -meson data from LHCb and assessing the impact of nuclear corrections and heavy-quark mass effects. The calculations presented here should play an important role in the interpretation of future data from neutrino telescopes such as IceCube and KM3NET, and highlight the opportunities that astroparticle experiments offer to study the strong interactions.

Contents

1	Introduction	1
2	Theoretical formalism	3
2.1	Neutrino-nucleon deep-inelastic scattering	4
2.2	Numerical implementation	6
2.3	Heavy-quark mass effects	8
2.4	Impact of nuclear modifications	10
3	Constraining small-x resummed PDFs with D-meson data	13
3.1	Fit settings, experimental data, and theory calculations	14
3.2	Results and validation	16
4	The neutrino-nucleon cross-section at ultra-high energies	20
4.1	Impact of theory settings and perturbative stability	20
4.2	Comparison to previous calculations	22
4.3	Comparison to IceCube data and impact of nuclear corrections	24
5	Summary and outlook	26
A	The BGR18 UHE neutrino-nucleus cross-sections	27
	References	31

1 Introduction

Ultra-high energy (UHE) neutrinos represent a unique messenger for a wide variety of astrophysical and cosmological phenomena [1–3]. Being charge-neutral, neutrinos are not deflected by galactic magnetic fields, while being weakly interacting implies that they are not attenuated *e.g.* by dust. Therefore, neutrinos point directly to their original source of production, offering crucial information which would be not available from other messengers such as electromagnetic waves or cosmic rays. This potential is illustrated by the recent report of the detection of UHE neutrinos from the same direction as a known Blazar [4].

UHE neutrinos also represent a very promising probe of physics beyond the Standard Model [5], for instance testing scenarios where PeV neutrinos arise from heavy dark matter decays [6] or those where neutrinos have non-standard interactions (NSI) [7]. Moreover, neutrino-nucleon scattering at very high energies also provides unique opportunities to test Quantum Chromodynamics (QCD) in an extreme kinematic regime far from those accessible at colliders [8].

At very high energies, the astrophysical neutrino flux Φ_ν decreases steeply with the neutrino energy E_ν with a power-law of approximately E_ν^{-2} [9]. The fact that the incoming UHE neutrino flux is so small, combined with the very feeble interactions of neutrinos with matter, makes the detection of UHE neutrinos extremely challenging. To bypass these limitations, neutrino telescopes such as IceCube [10], KM3NET [11], and Baikal [12] instrument large volumes of ice or water, which then act as detectors with an effective volume of up to 1 km³. This way, by accumulating data taken during several years, neutrino telescopes are expected to be able to detect neutrinos with energies as high as $E_\nu \simeq 10^{12}$ GeV. In addition, UHE neutrinos can also be studied by means of an array of radio antennas [13] or with balloon experiments such as ANITA [14].

Irrespective of the specific detection method adopted, the physical interpretation of the UHE neutrino event rates relies on an accurate theoretical prediction for the relevant signal process. In the case of the neutrino telescopes described above, the signal arises from the interaction [8] of a highly energetic neutrino with a nucleon from the target material, typically an H₂O molecule. The prediction for this scattering process is sensitive to both perturbative and non-perturbative QCD effects including the quark and gluon content of the target nucleon [15, 16], the treatment of heavy-quark mass effects [17], and the stability of the perturbative expansion at small values of the partonic momentum fraction x [18]. The sensitivity of the prediction to QCD dynamics represents both a challenge and an opportunity, given that the strong interactions must be probed in an unexplored kinematic regime. It is the main goal of this work to present a state-of-the-art calculation, taking into account recent developments in our understanding of perturbative and non-perturbative QCD, for the UHE neutrino-nucleon cross-section relevant for signal detection at neutrino telescopes. While a number of calculations have been provided by different groups in the past, both in the framework of collinear DGLAP factorisation [8, 19–24] and beyond it [25–30], there are now several significant motivations to revisit this calculation. The improvements made in this work, and their motivation, are detailed below.

Firstly, we account for the effects of small- x (BFKL) resummation up to the next-to-leading logarithm (NLL x) accuracy in the calculation of deep-inelastic scattering (DIS) structure functions and in the collinear evolution of parton distribution functions (PDFs). Specifically, the fixed-order calculations at next-to-next-to-leading order (NNLO) are consistently matched to the corresponding resummed results [31, 32]. Small- x corrections to the DIS structure functions are provided in the framework of the FONLL general-mass scheme [17, 33]. Recently, evidence for the onset of small- x resummation has been found [34, 35] in the inclusive and charm HERA data following the approach proposed in Refs. [36, 37]. It is thus of the utmost importance to include these effects also in the computation of the UHE cross-sections, which probe much smaller values of x than at HERA, down to $x \simeq 10^{-8}$.

Secondly, we include the constraints on PDFs arising from the LHCb D -meson production measurements in pp collisions at 5, 7, and 13 TeV [38–40] following the approach of Ref. [41]. As demonstrated in this work, and in the previous studies [42–44], the LHCb data provides important constraints at small- x which are in turn relevant for the UHE cross-section predictions. Here we revisit the study of Ref. [41] to account for the impact that

this data has on the PDFs extracted from a global analysis where small- x resummation effects have been included [34]. As will be shown, including the LHCb D -meson measurements leads to a significant reduction of the uncertainties on the UHE cross-sections associated to PDFs. It is worth mentioning that the same PDF constraints are also an important ingredient in the prediction of the so-called prompt neutrino flux [45], induced by the decays of D mesons produced in cosmic ray collisions in the atmosphere. The neutrinos produced in this process are a dominant background source in the search for UHE neutrinos of astrophysical origin. See Refs. [43, 46, 47] for more details as well as a number of related studies [48–54].

Finally, as the signal process of interest is neutrino scattering on an H_2O target (as opposed to a free nucleon), we account for nuclear modifications in the UHE cross-section predictions. There have been a number of studies quantifying the impact that nuclear modifications have on the distribution of quarks and gluons within bound nuclei in Refs. [55–58], which can be used to study the impact that nuclear corrections have on neutrino-nucleon scattering. These modifications (and the associated uncertainty) are absent from many of benchmark UHE cross-section calculations.

Our results represent a significant improvement over previous calculations of the UHE cross-sections both in terms of the perturbative (NNLO accuracy, small- x resummation) and non-perturbative (PDF constraints from D -meson data, nuclear corrections) content. This allows us to provide a more reliable comparison to the very recent direct measurements of the neutrino-nucleus interaction cross-sections at high energies [59, 60] extracted from the IceCube data, and to extrapolate the calculation to as of yet unexplored energies. Our calculations are made publicly available at the level of the total cross-section for a large range of (anti)neutrino values up to 10^{12} GeV. In addition, we also provide predictions for the DIS structure functions in the form numerical grids. These grids (with the relevant interpolation routines) may be used to construct a double-differential cross-section and can also be integrated numerically to obtain the total cross-section.

The outline of this paper is as follows. In Sect. 2 we present the theoretical formalism adopted for the calculation of the cross-sections. In Sect. 3 we revisit the impact of the LHCb D -meson data on the small- x PDFs once the effects of small- x resummation are accounted for. The main results of this work are presented in Sect. 4, where we also discuss the various sources of theoretical uncertainties associated to our calculation. We conclude in Sect. 5 and outline possible future developments. Appendix A contains a tabulated version of our calculation for the UHE cross-sections with the corresponding uncertainties, and also includes a description of the structure function grids and how they may be used to construct UHE cross-section predictions at both differential and integrated levels.

2 Theoretical formalism

In this section we present an overview of the theoretical settings used throughout this work to compute the UHE neutrino-nucleus cross-sections. We first review the basic ingredients required to evaluate predictions for neutrino-induced DIS cross-sections, focussing on the kinematic region relevant to UHE neutrino-nucleus scattering. We then provide details on

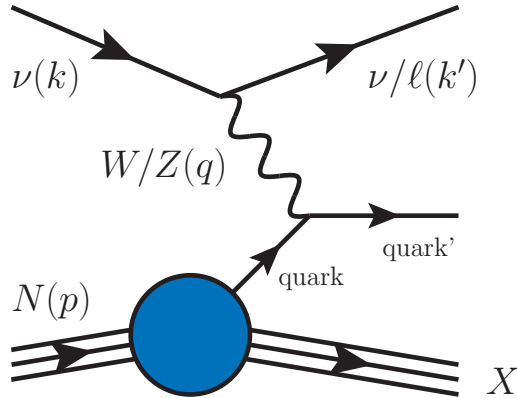


Figure 2.1. Diagram for deep-inelastic neutrino-nucleon scattering. The process proceeds through the exchange of an electroweak gauge boson either neutral (Z) or charged (W^\pm).

the theoretical accuracy and implementation of our calculation. Finally, we discuss the role played by heavy-quark mass effects and the treatment of nuclear corrections.

2.1 Neutrino-nucleon deep-inelastic scattering

As illustrated in Fig. 2.1, a high-energy neutrino interacts with a nucleon from the target through the exchange of an electroweak gauge-boson, either neutral (Z) or charged (W^\pm). The energy of the incoming neutrino can then be reconstructed by the energy deposited in the detector by either the outgoing lepton, in charged-current (CC) scattering, or the recoiling hadronic system in the case of neutral-current (NC) scattering.

The formalism for describing both NC and CC processes is equivalent, and in the following we focus on the CC case, $\nu(k) + N(p) \rightarrow \ell^\pm(k') + X(W)$. Details on the implementation of the NC case are discussed in Appendix A. The differential cross-section for this process can be written in terms of DIS structure functions as follows:

$$\frac{d^2\sigma_{\nu(\bar{\nu})N}^{\text{CC}}(x, Q^2, E_\nu)}{dx dQ^2} = \frac{G_F^2 M_W^4}{4\pi x(Q^2 + M_W^2)^2} \times \left(Y_+ F_{2,\text{CC}}^{\nu(\bar{\nu})N}(x, Q^2) \mp Y_- x F_{3,\text{CC}}^{\nu(\bar{\nu})N}(x, Q^2) - y^2 F_{L,\text{CC}}^{\nu(\bar{\nu})N}(x, Q^2) \right), \quad (2.1)$$

where the sign of the $x F_3$ term is positive (negative) for (anti)neutrino scattering, and N represents the struck nucleon.¹ In Eq. (2.1) we have defined $Y_\pm = 1 \pm (1 - y)^2$ and the DIS

¹In the case of (anti)neutrino scattering on an H_2O molecule, the total structure function can be obtained as the combination of that for a free proton (hydrogen) and that for bound nucleons within an oxygen nucleus. We will return to this point in Sect. 2.4.

kinematic variables are given by

$$Q^2 = -q^2, \quad y = \frac{q \cdot p}{k \cdot p} = 1 - \frac{E'}{E_\nu}, \quad x = \frac{Q^2}{2q \cdot p} = \frac{Q^2}{2m_N y E_\nu},$$

$$W^2 = (p + q)^2 = m_N^2 + Q^2 \left(\frac{1}{x} - 1 \right), \quad s = (k + p)^2 = m_N^2 + 2E_\nu m_N, \quad (2.2)$$

where some of the Lorentz-invariant quantities are also given in the laboratory centre-of-mass frame where the target nucleon is at rest. In these expressions, m_N is the nucleon mass, E_ν and E' are the incoming- and outgoing-lepton energies, and k , q , and p are the four-momenta of the neutrino, the gauge boson, and the nucleon (see Fig. 2.1).

The main ingredients for the theoretical prediction of the double-differential cross-section defined in Eq. (2.1) are the structure functions $F_{i=2,3,L}^{\nu(\bar{\nu})N}(x, Q^2)$, which describe the underlying QCD dynamics of the scattering process. Structure functions factorise as follows:

$$F_i(x, Q^2) = \sum_{a=g,q} \int_x^1 \frac{dz}{z} C_{i,a} \left(\frac{x}{z}, Q^2 \right) f_a(z, Q^2), \quad (2.3)$$

corresponding to the convolution of the universal PDFs (f_a) with the process-dependent coefficient functions ($C_{i,a}$). Typically, coefficient functions are computed in perturbation theory as a truncated expansion in powers of the strong coupling α_s .

Before discussing the theoretical accuracy of the structure function predictions, it is useful to illustrate the kinematic coverage of the UHE neutrino-nucleon cross-section for some representative values of the incoming neutrino energy E_ν . To do so, we compute the total CC neutrino-nucleon cross-section integrating Eq. (2.1) over the relevant kinematic region. The computation is performed at NLO using the NLO fixed-order NNPDF3.1sx central PDF set [34] assuming an isoscalar target.²

Fig. 2.2 shows the integration regions on the $(\log_{10}x \text{ vs. } \log_{10}Q^2)$ plane that contribute most (20%, 40%, 60%, and 80%) to the total cross-section for $E_\nu = 5 \times 10^8$ GeV (left) and $E_\nu = 5 \times 10^{10}$ GeV (right). The dot-dashed diagonal line indicates the upper bound of the integration of Q^2 as a function of x , that is given by $Q_{\max}^2(x) = 2m_N E_\nu x$. For $E_\nu = 5 \times 10^8$ (5×10^{10}) GeV, the main contribution to the cross-section arises from the region with $Q^2 \simeq M_W^2$ and $x \simeq 2 \times 10^{-5}$ (2×10^{-7}), with sensitivity to the small- x region down to $x \simeq 10^{-6}$ (10^{-8}). This pattern is the consequence of two separate effects. For $Q^2 \gg M_W^2$ the contribution to the total cross-section is power-suppressed by the W -boson propagator, see Eq. (2.1). For $Q^2 \ll M_W^2$, instead, the suppression of the cross-section is driven by the decrease of PDFs as Q^2 decreases.

In the kinematic regions highlighted in Fig. 2.2, fixed-order calculations are affected by the presence of large logarithms of x that spoil the perturbative convergence, see Refs. [31, 32, 61] and references therein. However, it has been shown that fixed-order calculations

²That is, a nucleus assumed to be composed of equal numbers of free protons and neutrons and where nuclear effects are neglected. The PDFs for such a nucleon can be obtained by assuming isospin symmetry to connect protons and neutrons.

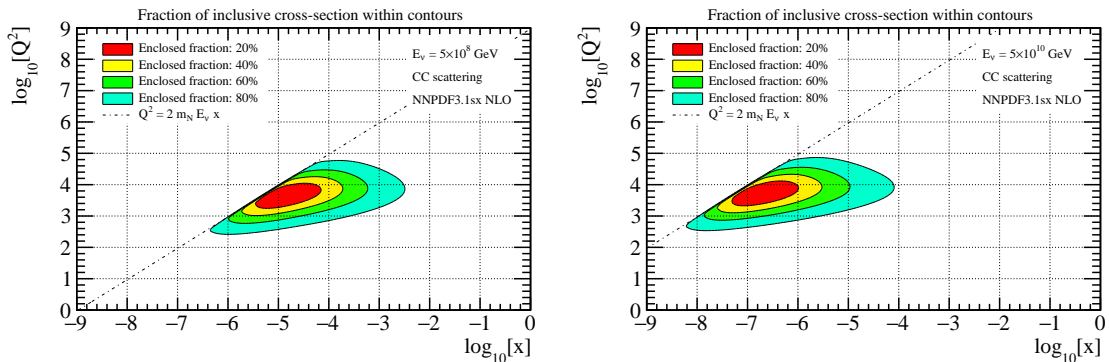


Figure 2.2. The percentage of the total UHE neutrino-isoscalar cross-section corresponding to the contribution of different kinematic regions in the (x, Q^2) plane in CC scattering. Predictions are computed in the FONLL scheme at NLO using the NNPDF3.1sx NLO PDF set. Results are shown for $E_\nu = 5 \times 10^8$ GeV (left) and $E_\nu = 5 \times 10^{10}$ GeV (right). The dot-dashed diagonal lines correspond to the kinematic limit $Q_{\max}^2(x) = 2m_N E_\nu x$.

can be complemented by small- x resummation effects to extend their validity down to very small values of x . Remarkably, this leads to a marked improvement in the description of the precise HERA 1+2 combined data [34, 35]. It is therefore important to account for these effects when computing predictions for the UHE neutrino-nucleus cross-section. As discussed below, predictions for the DIS structure functions in this work are accurate to NNLO+NLL x .

2.2 Numerical implementation

The DIS structure functions appearing in Eq. (2.3) are computed at fixed-order with the APFEL program [62]. APFEL has been interfaced to the HELL code [31, 32, 61] that provides small- x resummation corrections to the DIS coefficient functions and the DGLAP splitting functions. The computation of the structure functions is performed with the NNPDF3.1sx sets obtained in the corresponding global PDF analysis [34]. Heavy-quark mass effects are included in the calculation of the structure functions using the FONLL general-mass variable flavour number scheme [17, 33]. In the NC case, the FONLL-B and -C variants have been used for the NLO and NNLO computations, respectively. In the case of CC interactions, NNLO corrections to the massive coefficient functions have recently been computed [63] (see also Ref. [64]). However, the results of this calculation have not been made publicly available yet in a format suitable for the present calculation. Mass effects to the CC structure functions are therefore taken into account only up to NLO accuracy [65].

The numerical values of the heavy quark masses are the following: $m_c = 1.51$ GeV, $m_b = 4.92$ GeV, and $m_t = 172.5$ GeV. As for the electroweak parameters appearing in Eq. (2.1), we take: $M_W = 80.385$ GeV, $M_Z = 91.1876$ GeV, $G_F = 1.663787 \cdot 10^{-5}$ GeV $^{-2}$. For the CC interactions, we use a non-diagonal CKM matrix with the following absolute values: $|V_{ud}| = 0.97427$, $|V_{us}| = 0.22536$, $|V_{ub}| = 0.0035$, $|V_{cd}| = 0.22522$, $|V_{cs}| = 0.97343$, $|V_{cb}| = 0.04140$, $|V_{td}| = 0.00886$, $|V_{ts}| = 0.04050$, $|V_{tb}| = 0.99914$. This setup is consistent

with that adopted in the NNPDF3.1sx analysis.

For a number of phenomenological applications, such as the calculation of event rates at neutrino telescopes using Monte Carlo simulations, the double-differential distribution in Eq. (2.1) is the most relevant physical quantity. To this end, predictions for both CC and NC structure functions differential in x and Q^2 are made publicly available in the form of interpolation grids (see Appendix A).

However, the total neutrino-nucleon cross-section is also a highly relevant quantity for a number of analyses at neutrino telescopes. To construct the theoretical predictions for this quantity, it is necessary to integrate Eq. (2.1) over the allowed kinematic range in x and Q^2 . The total cross-section is therefore computed as

$$\sigma(E_\nu) = \int_{Q_{\min}^2}^{Q_{\max}^2} dQ^2 \left[\int_{x_0(Q^2)}^1 dx \frac{d^2\sigma}{dx dQ^2}(x, Q^2, E_\nu) \right]. \quad (2.4)$$

This integral is evaluated numerically using Gauss quadrature as implemented in `GSL` with relative precision set to 10^{-4} . Results were cross-checked by comparing to those obtained by performing a two-dimensional Monte Carlo integration with the `VEGAS` algorithm (as implemented in the `CUBA` library [66]) and requiring a relative precision of 5×10^{-3} .

The integration limits of the integrals in Eq. (2.4) are obtained by inspection of the DIS kinematics in Eq. (2.2). The inelasticity y is bounded within the range of $y \in [0, 1]$, and consequently the maximum value that Q^2 can take for a given neutrino projectile energy is given by $Q_{\max}^2 = 2m_N E_\nu$. While the integration in Q^2 in Eq. (2.2) should extend all the way down to zero, it is in practice necessary to impose a cut so that the structure functions are evaluated in the region of validity of perturbation theory. We choose $Q_{\min}^2 = Q_0^2$, where Q_0 is the scale at which the input PDFs are parameterised. In the case of NNPDF3.1sx, $Q_0 = 1.64$ GeV. As far as the integration over x is concerned, the upper integration bound is naturally set to one, while the lower bound for each particular value of Q^2 should be set to $x_0(Q^2) = Q^2/(2m_N E_\nu)$. However, when E_ν becomes very large and for values of Q^2 close to Q_{\min}^2 , x_0 can potentially become very small. Since we cannot access PDFs down to indefinitely small values of x , we need to impose a cut on the minimum value that x_0 can take. To this end, we replace the lower bound of the integration in x in Eq. (2.4) with $x_0(Q^2) = \max[Q^2/(2m_N E_\nu), x_{\min}]$. For our nominal results we choose $x_{\min} = 10^{-9}$.

In order to investigate the dependence of the results on the integration limits Q_{\min}^2 and x_{\min} , we have computed the total CC neutrino cross-section on an isoscalar target as a function of incoming neutrino energy E_ν for different values of Q_{\min}^2 and x_{\min} . The results are shown in Fig. 2.3 where the cross-section is computed at NLO for different values of Q_{\min}^2 (left) and x_{\min} (right), presented as a ratio to that obtained with the nominal values of $Q_{\min} = 1.64$ GeV and $x_{\min} = 10^{-9}$. Regarding the dependence on the value of x_{\min} , we find that the total cross-section becomes sensitive to the precise value of x_{\min} only for extremely large energies ($E_\nu \gtrsim 10^{10}$ GeV). For instance, at $E_\nu = 10^{12}$ GeV the total cross-section is reduced by around 15% if the integration is restricted to $x_{\min} = 10^{-7}$ as compared to the nominal value $x_{\min} = 10^{-9}$. With respect to the choice of Q_{\min} , we find that the total cross-section receives non-negligible contributions from the region $Q \in [1.64, 2.2]$ GeV for neutrino energies below $E_\nu \lesssim 5 \times 10^3$ GeV. For instance, raising

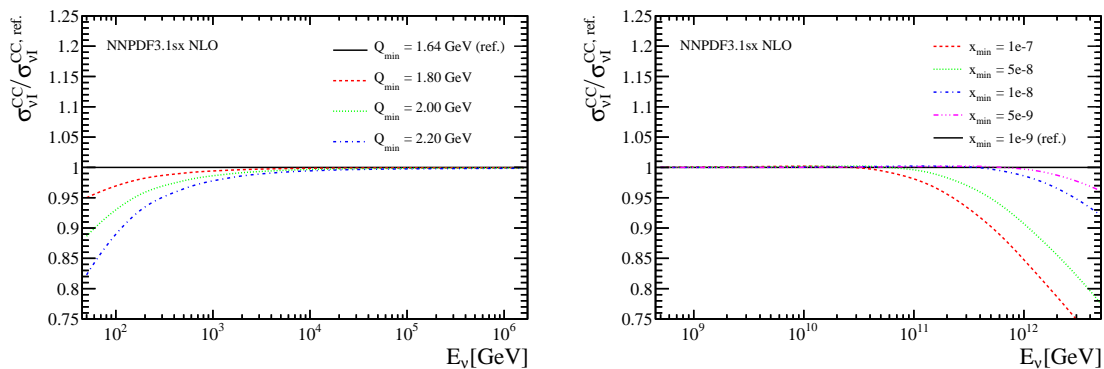


Figure 2.3. The dependence of the total CC neutrino-isoscalar cross-section, Eq. (2.4), with respect to variations of the lower integration limits Q_{\min}^2 (left) and x_{\min} (right) presented as ratios to the default (ref.) values.

Q_{\min} from the nominal value of 1.64 GeV up to 2.2 GeV leads to a suppression of the total cross-section by around 15% at $E_\nu = 100$ GeV. The predictions provided in this work can thus be considered reliable for neutrino energies $E_\nu \gtrsim 5 \times 10^3$ GeV. Accurate predictions in the region $E_\nu \lesssim 5 \times 10^3$ GeV could be achieved by matching the perturbative QCD calculation of the structure functions to a parameterisation of low- Q^2 neutrino structure functions [67], following for instance the approach developed in Ref. [68].

2.3 Heavy-quark mass effects

Previous calculations of the UHE neutrino-nucleon cross-sections have been performed in the zero-mass variable-flavour-number scheme (ZM-VFNS), where finite mass effects in the computation of the partonic cross-sections are neglected. Nonetheless, it is now well known that heavy-quark mass effects are required in order to provide an adequate description of the HERA data in the low- Q^2 region. Since the computation of the total neutrino cross-sections requires integrating over a wide range in Q^2 that includes the regions close to the charm- and bottom-quark masses, heavy-quark mass corrections can be relevant. As mentioned above, our predictions for the DIS structure functions are computed using the FONLL scheme that accounts for heavy-quark mass effects. In the following, we assess the importance of including these effects in the UHE cross-section predictions. We also discuss the relevance of top-quark mass effects.

We first consider the impact of charm- and bottom-quark mass effects on both the CC and NC calculations at the level of the single-differential cross-section $d\sigma/dQ^2$. This is obtained by integrating Eq. (2.1) over the allowed kinematic range of x , namely

$$\frac{d\sigma(Q^2, E_\nu)}{dQ^2} = \int_{x_0(Q^2)}^1 dx \frac{d^2\sigma}{dx dQ^2}(x, Q^2, E_\nu). \quad (2.5)$$

In Fig. 2.4 we consider the predictions for the differential DIS cross-section in Eq. (2.5) in the CC (left) and in the NC (right) case. Predictions are computed as functions of Q^2 at $E_\nu = 10^7$ GeV at NLO in both the FONLL scheme and the ZM-VFNS. The upper panels

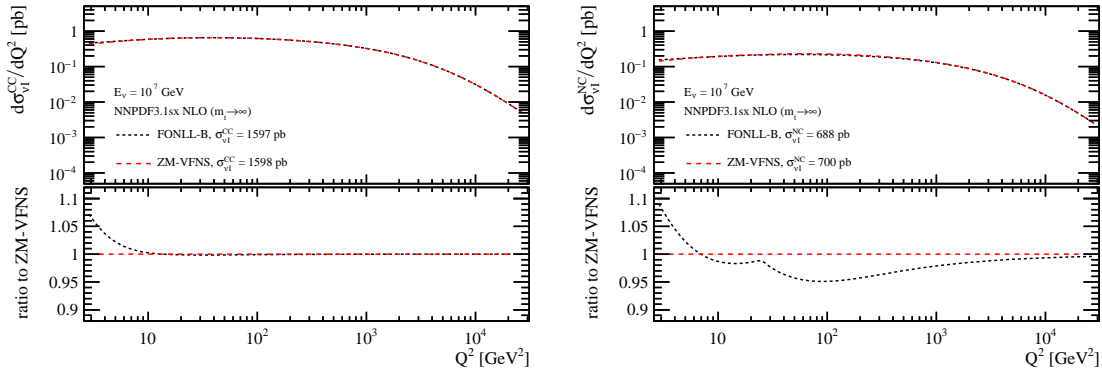


Figure 2.4. Comparison between the FONLL and ZM-VFN heavy-quark mass schemes at NLO for the calculation of the single-differential cross-section $d\sigma_{\nu I}/dQ^2$, Eq. (2.5), for CC (left) and NC (right) scattering at $E_\nu = 10^7$ GeV. In both cases the limit $m_t \rightarrow \infty$ is taken to decouple the effects of the top quark.

display the absolute distributions while the lower panels show the ratio to the ZM-VFNS. In these plots the limit $m_t \rightarrow \infty$ is taken to decouple the effect of the top quark.³ In the upper panel of these plots, the total cross-section obtained by integrating over the allowed range in Q^2 is also reported.

In the case of CC scattering, the inclusion of charm-mass effects introduces a positive shift of up to 5% in the region of $Q^2 \lesssim 10$ GeV² but has a negligible impact on the total cross-section. The impact of bottom-mass effects is entirely negligible. This is due to the strong suppression for the subprocesses involving the CKM matrix elements V_{ub} and V_{cb} . Heavy-quark mass corrections in NC case display a similar behaviour at low energies but introduce a negative correction in the intermediate energy range of $Q^2 \in [20, 500]$ GeV². The net effect is a reduction of the total cross-section by (1-2)%. While not shown here, similar results are also obtained for neutrino energies in the range $E_\nu \in [10^3, 10^{12}]$ GeV. From this comparison, we conclude that charm- and bottom-quark mass effects are negligibly small at the level of the total cross-section, but may still be relevant for the calculation of the double-differential distributions in Eq. (2.1). These effects are included in our predictions unless specifically stated.

In addition to charm- and bottom-quark mass effects, it is also important to consider the mass effects related to the top quark (see also Ref. [69]). The Born processes for massive top-quark production in neutrino-nucleon scattering are

$$\text{CC : } \nu + q_d \rightarrow \ell^- + t, \quad \text{NC : } \nu + g \rightarrow \ell^- + t + \bar{t}, \quad (2.6)$$

where in the CC process q_d denotes a down-type quark. Kinematically, the CC (NC) process may only proceed if the *physical* threshold for the production of a top quark (pair) is reached, namely

$$W^2 = \frac{Q^2(1-x)}{x} > m_t^2 \quad (W^2 > 4m_t^2), \quad (2.7)$$

³This is done for illustration purposes only. Finite m_t effects are included in our calculation, see the discussion below.

where the target nucleon mass is neglected. An accurate prediction for these processes relies on the inclusion of mass effects in the partonic cross-section. We account for these effects by adopting the FONLL scheme with a maximum of $n_f = 6$ active flavours ($n_f = 6$ scheme, in short). In this scheme the top quark is treated as a massive parton for energies close to the top-quark mass, and becomes effectively massless at much larger energies, $Q^2 \gg m_t^2$. This has the consequence of introducing top-quark PDFs whose evolution resums potentially large logarithms of the form $\ln(Q^2/m_t^2)$. As discussed in Sect. 2.2, heavy-quark mass effects are accounted for at $\mathcal{O}(\alpha_s^2)$ for NC scattering and $\mathcal{O}(\alpha_s)$ for CC scattering. We note that the scheme choice in this work contrasts with the approach commonly used in the extraction of PDFs from experimental data, such as the NNPDF3.1sx sets used in this work, in which the $n_f = 5$ scheme is preferred. In order to employ the $n_f = 6$ scheme, we have generated variants of the NNPDF3.1sx sets in which the top-quark PDFs are dynamically generated at $Q^2 = m_t^2$ [70]. These sets coincide with the original ones for $Q^2 < m_t^2$ and are made publicly available (see Appendix A).

In Fig. 2.5 we assess the impact of top-quark production on the total cross-section for both CC (left) and NC (right) scattering. To do so, cross-sections are computed at NLO in the $m_t \rightarrow \infty$ limit and compared to the default $n_f = 6$ FONLL calculation with $m_t = 172.5$ GeV. Taking the limit of $m_t \rightarrow \infty$ effectively increases the production threshold for top production such that it becomes kinematically inaccessible. Comparing these predictions is therefore useful to single out the relative contribution for the top-quark production to the total cross-section.

For CC scattering (left plot of Fig. 2.5), it is found that the top-quark contribution becomes relevant for neutrino energies of $E_\nu \gtrsim 10^7$ GeV, while for NC scattering (right plot) the contribution is negligible. Inspection of Eq. (2.7) reveals that the production of a single top-quark in CC scattering is kinematically possible for $Q^2/x \gtrsim m_t^2$. Therefore, for neutrino energies of $E_\nu \gtrsim 10^7$ GeV top-quark production becomes accessible at relatively small values of Q^2 in the low- x region. This process is dominated by the partonic subprocess $W + b \rightarrow t$ as a consequence of the steep growth of the b -quark PDF (generated at $Q = m_b$) at low- x , and of the fact that $|V_{tb}| \approx 1$. The combination of these effects results in a non-negligible contribution to the total CC cross-section which represent up to 5% of the total cross-section at $E_\nu \sim 10^{12}$ GeV.

2.4 Impact of nuclear modifications

At neutrino telescopes, the incoming UHE neutrinos scatter upon nucleons which may be bound within a nucleus of the target material. Therefore, in principle it is necessary to account for the presence of nuclear-binding effects. The most relevant of these effects for the calculation of the UHE cross-sections is that of shadowing [71], namely the depletion of nuclear structure functions as compared to their free-nucleon counterparts. In experiments such as IceCube, KM3NET, and Baikal the nuclear target is a molecule of H_2O , and the scattering is dominated by bound nucleons inside the oxygen nuclei with a small admixture of the free protons from the hydrogen.

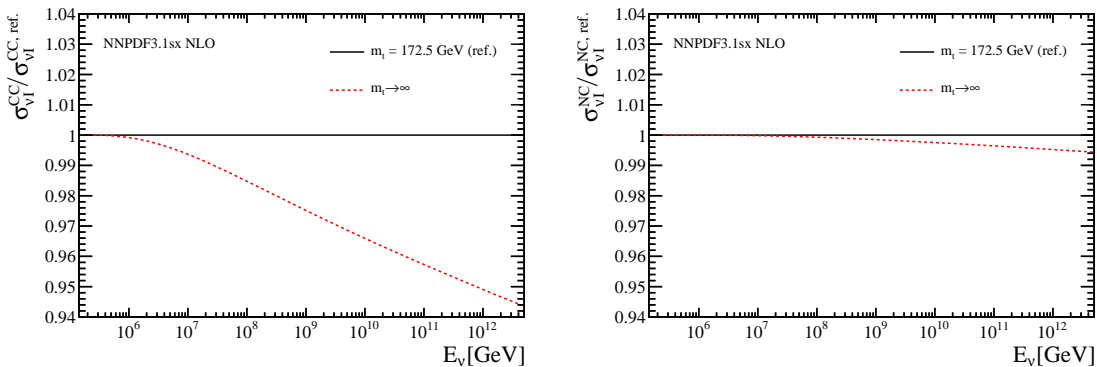


Figure 2.5. The ratio of the CC (left) and NC (right) neutrino-isoscalar cross-section at NLO computed in the $m_t \rightarrow \infty$ limit compared with our default (ref.) $n_f = 6$ FONLL calculation with $m_t = 172.5$ GeV.

The mass-averaged structure function for a water/ice target may thus be written as

$$F^{\text{H}_2\text{O}} = \frac{1}{2 + A} (2F^p + ZF^{p,A} + NF^{n,A}), \quad (2.8)$$

where F^p is the structure function of a free proton, and $F^{p(n),A}$ represents that of a proton (neutron) which is bound within a nucleus with mass number A containing Z protons and N neutrons, with $A = Z + N$. In this case, the bound nucleus is that of oxygen which is an isoscalar target ($N = Z$) with $A = 16$. Predictions for these structure functions can be computed according to Eq. (2.3), where the PDFs correspond to those of the (bound) nucleon. This implies that one should account for the effects that quark and gluon PDFs of a nucleon experience inside a heavy nucleus. These corrections have been quantified in a number of analyses of nuclear parton distribution functions (nPDFs) [55–58].

To assess the impact of nuclear corrections on the UHE neutrino-nucleon cross-sections, we have computed the mass-averaged total cross-section for an H_2O molecule using the nPDFs from the EPPS16 global analysis [56]. These predictions are obtained by first computing the cross-section for both a free proton and an oxygen target, and then performing a combination according to

$$\sigma_{\nu\text{H}_2\text{O}}(E_\nu) = \frac{1}{18} (2\sigma_{\nu p}(E_\nu) + \sigma_{\nu O}(E_\nu)). \quad (2.9)$$

The EPPS16 fit is constructed taking the CT14 NLO free-nucleon PDFs [72] as a baseline. Therefore, we use the central value of this PDF set for the free-nucleon predictions.⁴ Results for both CC and NC scattering cross-sections (for the sum of neutrino- and antineutrino-induced processes) are shown in Fig. 2.6. Distributions are presented as normalised to those of the corresponding free-nucleon predictions. The quoted uncertainty bands represent the 1σ uncertainty of the EPPS16 set (excluding free-nucleon uncertainties) evaluated using the asymmetric Hessian prescription.

⁴In the numerical computation, we also adjust the values of Q_{\min} and x_{\min} values to match those of EPPS16.

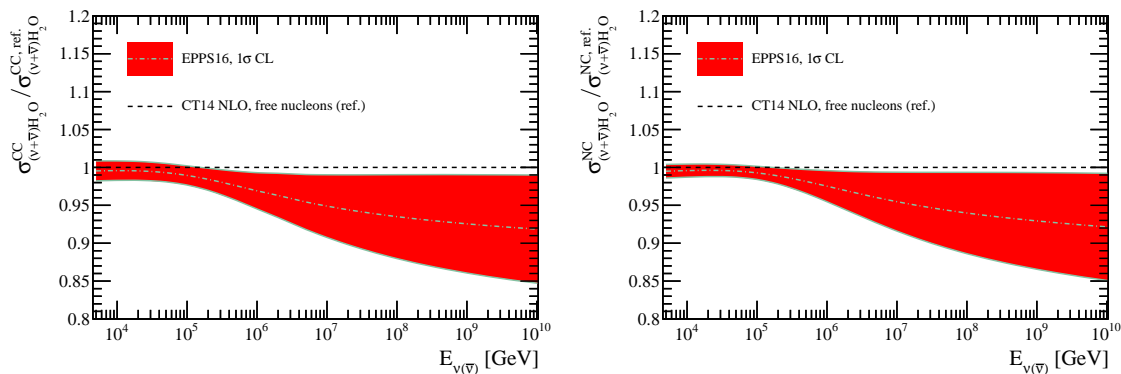


Figure 2.6. The CC (left) and NC (right) neutrino-nucleon cross-sections (adding the contributions from neutrinos and antineutrinos) for an H_2O molecule computed with the EPPS16 nPDF set and presented as a function of the neutrino projectile energy $E_{\nu(\bar{\nu})}$. The quoted 1σ confidence-level (CL) uncertainty bands include only the uncertainty from the nuclear PDF fit, and have been evaluated using the asymmetric Hessian prescription. Each distribution has been normalised with respect to the baseline free-nucleon prediction.

We find a suppression of the cross-section for (anti)neutrino energies $E_{\nu(\bar{\nu})} \gtrsim 10^6$ GeV due to the shadowing effect present in the nPDFs at small- x . The central value is reduced by 3% for $E_{\nu(\bar{\nu})} = 10^6$ GeV, and by as much as 10% for $E_{\nu(\bar{\nu})} = 10^{10}$ GeV. However, it should be noted that while a suppression of the cross-section is preferred, the uncertainty of the nuclear corrections are almost as large as the shift of the central value. Therefore, using EPPS16, the significance of nuclear modifications is mostly within the 1σ level. At lower energies, instead, the impact of the nuclear corrections becomes less important. The results of Fig. 2.6 indicate that nuclear corrections represent a large source of theoretical uncertainty in the predictions of the UHE neutrino-nucleon cross-section. Therefore, it is necessary to account for such effects to provide reliable predictions.

In Sect. 4, where predictions are provided for the total UHE cross-sections, the impact of nuclear corrections is accounted for in a factorised form. To illustrate this procedure, we consider here the construction of the cross-section for the neutrino-induced scattering on an oxygen nucleus. First, the nuclear modification factor $R_{\nu O}(E_\nu)$ is computed with the EPPS16 nPDFs as follows:

$$R_{\nu O}(E_\nu) \equiv \left(\frac{\sigma_{\nu O}^{\text{EPPS16}}(E_\nu)}{\sigma_{\nu I}^{\text{free}}(E_\nu)} \right), \quad (2.10)$$

where $\sigma_{\nu I}^{\text{free}}(E_\nu)$ is the cross-section for an isoscalar target computed with the central CT14 NLO free-nucleon PDFs, and the normalisation is such that $R_{\nu O}(E_\nu) \rightarrow A = 16$ in the limit of vanishing nuclear effects. Note that the flavour symmetry of PDFs at small- x implies that Eq. (2.10) gives essentially the same results for both NC and CC scattering, as also seen from Fig. 2.6.

This modification factor is then applied to the cross-section for an isoscalar target computed with a different set of free-nucleon PDFs according to

$$\tilde{\sigma}_{\nu O}(E_\nu) = R_{\nu O}(E_\nu) \tilde{\sigma}_{\nu I}(E_\nu), \quad (2.11)$$

for either NC or CC scattering. The mass-averaged cross-section for neutrino scattering on a molecule of H₂O is obtained according to Eq. (2.9). In fact, for the highest neutrino energies, any departures from non-isoscalarity can be ignored and the following approximation can be made

$$\sigma_{\nu\text{H}_2\text{O}}(E_\nu) \simeq \frac{\sigma_{\nu I}(E_\nu)}{18}(2 + R_{\nu O}(E_\nu)). \quad (2.12)$$

The total uncertainty in Eq. (2.12) can then be computed by adding in quadrature the free-nucleon PDF uncertainties (arising from $\sigma_{\nu I}$) with those of the nPDFs (from $R_{\nu O}$).

The factorised expression in Eq. (2.12) makes it straightforward to improve the prediction of the total cross-section when a more precise determination of $R_{\nu O}(E_\nu)$ becomes available.⁵ The large uncertainties associated to $R_{\nu O}(E_\nu)$ in the current calculation can be related to the lack of experimental data used to determine nPDFs (and in particular those sensitive to the gluon) in the region of $x \lesssim 10^{-2}$. Indeed, to compute $R_{\nu O}(E_\nu)$ at large E_ν values it is necessary to extrapolate nPDFs to small values of x by several orders of magnitude. In the extrapolation region results are driven to a large extent by the particular methodological choices made to extract nPDFs. Examples are the parameterisation (*i.e.* the functional form assumed to parameterise the x and A dependence) or χ^2 tolerances that define the 1σ PDF uncertainties.⁶

As will become apparent in Sect. 4, the uncertainty associated to the nuclear corrections is a limiting factor in the calculation of the UHE neutrino-nucleon cross-section. This provides a strong motivation to improve global fits of nPDFs by extending the kinematic coverage of the input data set. One possibility is to include LHC data collected in $p+Pb$ collisions which are sensitive to the small- x region. The nPDFs are typically parameterised as continuous functions of the nucleus mass number A . Therefore, constraints obtained for nucleons bound within a Pb nucleus ($A = 208$) are relevant also for lighter nuclei such as oxygen. Progress in this direction may be possible by studying forward D -meson production in $p+Pb$ collisions [73], but these data have not yet been included in any nPDF fits (see Ref. [74] for initial work in this direction). In the longer term, stringent constraints would also be provided by possible future lepton-ion colliders such as the EIC [75] and the LHeC [76].

3 Constraining small- x resummed PDFs with D -meson data

The analysis of Ref. [41] quantified the impact of the LHCb D -meson cross-section measurements on the NNPDF3.0 NLO PDFs at small x . Here we revisit this analysis, applying it to the NNPDF3.1sx sets [34, 77] which have been extracted either with or without including the effects of small- x resummation. In this section, we review the fit settings and

⁵Another benefit of this factorised expression is that it is straightforward to calculate the nuclear correction for other nuclear targets. This may be relevant for the modelling of neutrino absorption within the Earth as neutrinos may scatter via the NC process on an Fe target [59].

⁶We have also repeated the analysis above using the nCTEQ15 nuclear PDF sets [57] and obtained consistent results. However, it was found that the 1σ uncertainties were considerably smaller as compared to the EPPS16 results. Therefore, we quote the EPPS16 results which provide a more conservative uncertainty estimate.

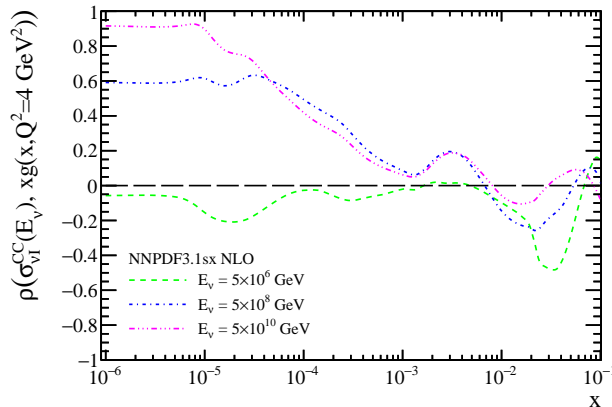


Figure 3.1. The correlation coefficient ρ between the gluon PDF at $Q^2 = 4 \text{ GeV}^2$ and the CC neutrino-isoscalar cross-section evaluated at specific values of E_ν , presented as a function of the momentum fraction x carried by the gluon.

discuss the experimental inputs along with the corresponding theoretical calculations used to include the LHCb data into the fit. We then present the fit results and describe the tests performed to assess their robustness.

3.1 Fit settings, experimental data, and theory calculations

The kinematic coverage of the UHE neutrino-nucleon cross-section as shown in Fig. 2.2 illustrates the sensitivity of this observable to PDFs in a region of extremely small x ($x \simeq 10^{-8}$). This region is outside the coverage of the input datasets used in the current PDF fits. In particular, it is beyond the coverage of the HERA data [78] that only reach values of x as small as $x \simeq 2 \times 10^{-5}$ for $Q^2 \gtrsim 1 \text{ GeV}^2$. However, recent work has demonstrated that smaller values of x can be probed using D -meson production measurements as provided by the LHCb experiment. Several groups have shown [42–44] that forward D -meson cross-section measurements can provide important information on both the normalisation and the shape of the small- x PDFs, especially that of the gluon. In particular, in Ref. [41] it has been shown that the combination of the LHCb measurements at $\sqrt{s} = 5, 7, \text{ and } 13 \text{ TeV}$ allows to substantially reduce the uncertainties of the gluon PDF at small x .

In order to illustrate the interplay between the small- x gluon PDF and the UHE neutrino-nucleon cross-sections, in Fig. 3.1 we show the correlation coefficient ρ [79] evaluated between the gluon PDF at $Q^2 = 4 \text{ GeV}^2$ and the CC neutrino-isoscalar cross-section $\sigma_{\nu I}^{CC}(E_\nu)$ for fixed values of E_ν . The correlation is shown as a function of the momentum fraction x carried by the gluon. Note that although there is no direct coupling between the electroweak bosons and the gluon, this correlation mostly arises from the impact of the latter on the sea quarks by means of the DGLAP evolution. From this comparison, we find a large correlation ($\rho \gtrsim 0.6$) in the small- x region ($x \lesssim 10^{-4}$) for the cross-section evaluated at large values of the neutrino energy $E_\nu \gtrsim 5 \times 10^8 \text{ GeV}$. Therefore, a better understanding of the small- x gluon PDF is necessary to obtain reliable predictions for the UHE neutrino-nucleon cross-sections in this energy range.

In this work we aim at providing predictions for the UHE neutrino-nucleon cross-sections using a state-of-the-art calculation based on structure functions accurate at NNLO+NLL x . This requires using PDFs extracted with the same accuracy. The main limitation in achieving this goal is that theoretical predictions for D -meson production are not available at this accuracy. Firstly, because NNLO differential cross-sections for heavy-quark pair production are only available for top quarks [80]. Secondly, because small- x resummed hard cross-sections [81] are not yet available in a form suitable for phenomenology.

Following Ref. [41], the impact of the LHCb D -meson production data on PDFs at small- x can be quantified by means of the following observables:

$$\begin{aligned} N_X^{ij} &= \frac{d^2\sigma(X \text{ TeV})}{dy_i^D d(p_T^D)_j} \bigg/ \frac{d^2\sigma(X \text{ TeV})}{dy_{\text{ref}}^D d(p_T^D)_j}, \\ R_{13/X}^{ij} &= \frac{d^2\sigma(13 \text{ TeV})}{dy_i^D d(p_T^D)_j} \bigg/ \frac{d^2\sigma(X \text{ TeV})}{dy_i^D d(p_T^D)_j}, \end{aligned} \quad (3.1)$$

where $X = 5$ or 7 , p_T^D and y^D are the transverse momentum and rapidity of the D mesons, and y_{ref}^D denotes a reference rapidity bin. Eq. (3.1) implies that we use D -meson differential distributions always in a normalised form, taking as a reference either a given rapidity bin or data taken at a different centre-of-mass energy. An important implication of this approach is that missing higher-order corrections to partonic cross-sections partially cancel in the ratios, reducing the sensitivity of these observables to such corrections. Crucially, numerators and denominators in Eq. (3.1) probe different regions in x , and therefore these observables still provide constraints on the PDFs at small x .

We apply Bayesian reweighting [82, 83] to prior PDF sets which have previously been extracted with different theory settings. Specifically, we use the NNPDF3.1sx sets based on: NLO, small- x resummation matched to NLO (*i.e.* NLO+NLL x), and small- x resummation matched to NNLO (*i.e.* NNLO+NLL x). In all cases, the partonic cross-sections for D -meson production are computed at NLO. We discuss below the stability of our results with respect to this choice.

For the PDF reweighting, we exploit the LHCb measurements of D -meson cross-section measurements in pp collisions at $\sqrt{s} = 5, 7, \text{ and } 13 \text{ TeV}$ [38–40]. These data are provided double differentially with respect to p_T^D and y^D for different types of D meson. The kinematic coverage of these cross-sections is approximately $p_T^D \in [0, 8] \text{ GeV}$ and $y^D \in [2, 4.5]$, with small differences depending on the specific D -meson species and the hadronic centre-of-mass energy. From these measurements we construct the two normalised observables defined in Eq. (3.1) for the D^0 , D^+ , and D_s species and the corresponding anti-particles.

In what follows we adopt as a baseline the results of the fit with the normalised cross-sections N_X^{ij} , denoted by N_{5+7+13} . The LHCb data is restricted to the region $p_T^D \in [1, 8] \text{ GeV}$. The reason for this cut is that in our calculation the factorisation and renormalisation scales are set equal to the transverse mass of the outgoing heavy quark. Since the NNPDF3.1sx fits are determined at the input scale of $Q_0 = 1.64 \text{ GeV}$, restricting to the region $p_T^D \in [1, 8] \text{ GeV}$ avoids sampling the PDFs outside their validity range. Practically, we set $\mu_{\text{min}} = 1.64 \text{ GeV}$ in the calculation which is relevant for a very small fraction of

events with $p_T^c \simeq 0$ GeV and $p_T^D > 1$ GeV. As summarised in Table 3.1, with this kinematic cut, a total of 78, 72, and 119 data points at 5, 7, and 13 TeV, respectively, are included in the fit.

Applying the reweighting procedure requires computing the theory predictions for the observables in Eq. (3.1) using the $N_{\text{rep}} = 100$ replicas of the NNPDF3.1sx sets. These predictions are obtained at NLO+PS accuracy using POWHEG [84–87] to match the fixed-order calculation [88] to the PYTHIA8 shower [89, 90] with the default MONASH 2013 tune [91]. The calculation is performed with an input value for the charm-quark mass of $m_c = 1.5$ GeV.

3.2 Results and validation

Following the procedure outlined above, we have produced three variants of the NNPDF3.1sx+LHCb fits, based on the NLO, NLO+NLL x , and NNLO+NLL x theory settings. In all cases, the matrix-elements for the partonic process are evaluated at NLO [88]. In Fig. 3.2 we compare the gluon PDF from the three prior NNPDF3.1sx sets at $Q^2 = 4$ GeV² with the corresponding results after the LHCb D -meson cross-sections have been included in the fit. For completeness, we also compare the NLO results which have been obtained with the NNPDF3.0+LHCb set [41]. PDF uncertainties are computed as 1σ intervals.

From the comparisons in Fig. 3.2 we find a significant reduction of the PDF uncertainties due to the inclusion of the LHCb D -meson cross-section data. The magnitude of this reduction turns out to be similar for all the three theory settings considered. We also observe that at NLO, consistent results are obtained for the two different priors, NNPDF3.0 and NNPDF3.1sx. This stability is reassuring taking into account the differences between the two fits in terms of input dataset, treatment of the charm quark PDF, and the values of the heavy-quark masses.

In the lower-right plot of Fig. 3.2 we also display the comparison of the three NNPDF3.1sx+LHCb sets based on NLO, NLO+NLL x , and NNLO+NLL x theory. The stability of the perturbative expansion once small- x resummation effects are accounted for is evident. Indeed, the differences between the central values of the NLO+NLL x and NNLO+NLL x gluon PDFs are always smaller than the corresponding uncertainties in the entire range of x considered. We also observe that the central value of the small- x gluon PDF is larger in the NNLL x case as compared to fixed-order and that the effective behaviour at small x is a moderate rise rather than a constant behaviour as at NLO.

In Table 3.1 we report the values of χ^2/N_{dat} for each of the LHCb D -meson datasets considered in this analysis. For each of the three theory settings considered, we show the results both before (χ_{orig}^2) and after (χ_{new}^2) adding the LHCb data into the fit. In the first column of this table, we also indicate the values of N_{dat} for each dataset. The results for the N_{5+7+13} combination, corresponding to $N_{\text{dat}} = 269$ data points, represent the baseline fit of this work. For completeness, we also provide the χ^2 values for the ratio between the cross-sections at 13 and 5 TeV, $R_{13/5}$.

From Table 3.1 one finds that an excellent description is obtained for the normalised D -meson cross-sections, with similar values of the χ^2/N_{dat} for the three different theory settings, and with the NLO+NLL x fit leading to the smallest χ_{new}^2 . As discussed in Ref. [41],

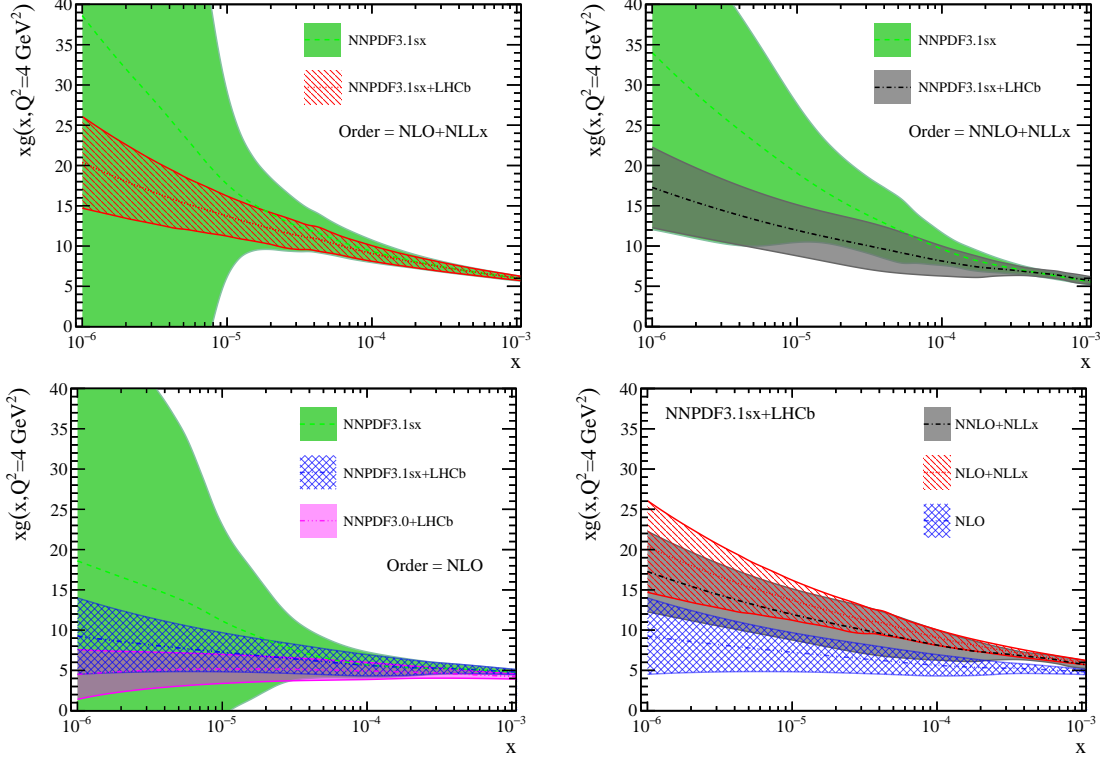


Figure 3.2. Comparison of the gluon PDF at $Q^2 = 4 \text{ GeV}^2$ from the different NNPDF3.1sx prior sets with the corresponding results once the LHCb D -meson cross-sections have been included in the fit. The results are shown for three different theoretical settings: using resummed NLO+NLL x and NNLO+NLL x theory (upper plots) and using fixed-order NLO theory (lower-left plot). In addition, a comparison of the fit results obtained with different theory settings is also shown in the lower right plot. For completeness, in the NLO comparison we also show the NNPDF3.0+LHCb results of Ref. [41].

in the calculation of these χ^2 values the experimental bin-by-bin correlation matrices are included for $R_{13/5}$, while for the normalised cross-section data these correlations (which are only available for N_5 and N_{13}) are not included.

In this analysis the partonic cross-sections for charm-quark production, convoluted with NLO and (N)NLO+NLL x accurate PDFs, are accurate to NLO in all cases. In order to assess the robustness of these results with respect to this approximation, the analysis of the N_{5+7+13} normalised cross-section dataset has been repeated in the following way. A modified χ^2 is introduced to quantify the agreement between theory and data, defined as

$$\chi_{\text{mod}}^2 = \sum_i \frac{(O_i^{\text{exp}} - O_i^{\text{th}})^2}{(\delta O_i^{\text{exp}})^2 + (\delta O_i^{\text{th}})^2}, \quad (3.2)$$

where O_i corresponds to the i -th bin value of the observable O and δO_i to its uncertainty. Note that in our baseline analysis the theoretical uncertainty δO_i^{th} is not accounted for. This estimator is then used to repeat the NLO+NLL x analysis, and in this case we define

	NLO		NLO+NLL x		NNLO+NLL x	
Dataset (N_{dat})	$\chi_{\text{orig}}^2/N_{\text{dat}}$	$\chi_{\text{new}}^2/N_{\text{dat}}$	$\chi_{\text{orig}}^2/N_{\text{dat}}$	$\chi_{\text{new}}^2/N_{\text{dat}}$	$\chi_{\text{orig}}^2/N_{\text{dat}}$	$\chi_{\text{new}}^2/N_{\text{dat}}$
N_5 (78)	1.0	0.71	1.11	0.78	1.61	0.84
N_7 (72)	0.8	0.69	0.84	0.72	0.96	0.75
N_{13} (119)	1.51	1.13	1.6	1.16	2.0	1.22
N_{5+7+13} (269)	1.17	0.89	1.25	0.93	1.61	0.98
$R_{13/5}$ (99)	1.64	1.66	1.87	1.79	1.83	1.74

Table 3.1. The values of the χ^2 per data point, χ^2/N_{dat} , for each of the LHCb D -meson production datasets considered in this analysis. Each centre-of-mass energy contains the results of all the D -meson species considered. For each of the three theory settings, we show the results both before (χ_{orig}^2) and after (χ_{new}^2) adding the LHCb data into the fit. In the first column we also indicate the values of N_{dat} for each dataset. In this work the results based on the N_{5+7+13} dataset are taken as the baseline.

the theory error δO_i^{th} to be the following shift

$$\delta O_i^{\text{th}} \equiv O_i^{\text{evNLO}} - O_i^{\text{evNLO+NLL}x}, \quad (3.3)$$

where the cross-section O_i^{evNLO} is evaluated by evolving upwards the NLO+NLL x NNPDF3.1sx set from $Q_0 = 1.64$ GeV to larger- Q values using fixed-order NLO evolution. The cross-section $O_i^{\text{evNLO+NLL}x}$ is instead evaluated using NLO+NLL x settings for the evolution. The same strategy can be applied to the NNLO+NLL x case, where Eq. (3.2) is written in terms of O_i^{evNNLO} and $O_i^{\text{evNNLO+NLL}x}$.

This additional source of theoretical uncertainty δO_i^{th} is introduced in the χ^2 in Eq. (3.2) in order to estimate the possible impact of the missing contributions in the evaluation of the hard cross-sections for charm production. It effectively reduces the contribution to the χ^2 due to those bins that are most sensitive to the difference between (N)NLO+NLL x and (N)NLO PDF evolution. Consequently, the weight of these bins is reduced in the reweighting procedure.

In Fig. 3.3 we show the same comparison as in the upper plots of Fig. 3.2, now normalised to the central value of the NNPDF3.1sx+LHCb baseline result and adding the results (indicated by a *) of the fits obtained using the modified definition for the χ^2 in Eq. (3.2). One finds that adding the additional theory uncertainty in the χ^2 leads to slightly larger PDF uncertainties together with a small positive shift of the central value, both at NLO+NLL x and at NNLO+NLL x . These results suggest that missing NLL x corrections in the prediction of the D -meson production cross-sections can be neglected as compared to the gluon PDF uncertainties, thus justifying the approximations used in this work.

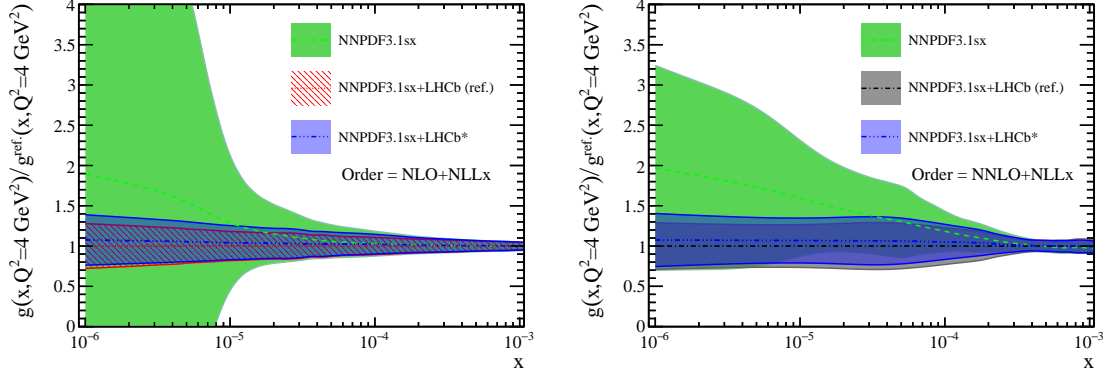


Figure 3.3. The same comparison as in the upper plots in Fig. 3.2, now normalised to the central value of the NNPDF3.1sx+LHCb baseline result and adding the results (indicated by a *) of the fits obtained using the modified definition for the χ^2 in Eq. (3.2).

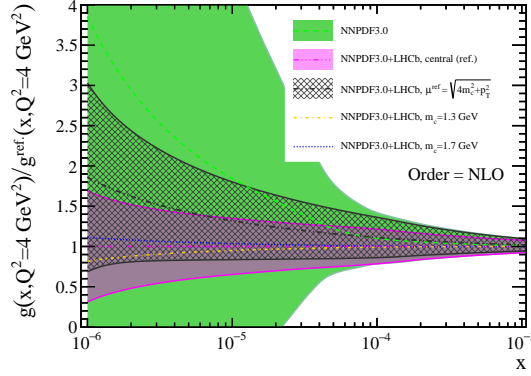


Figure 3.4. Same as Fig. 3.3 for the NNPDF3.0+LHCb fit, comparing the baseline results with those obtained varying the scale $\mu^{(\text{ref})}$ and the value of the charm mass m_c .

The results of the reweighting analysis are affected by further theoretical uncertainties, such as the choice of renormalisation and factorisation scales (set equal in this analysis) and of the value of the charm-quark mass used in the calculation of Ref. [41]. For illustration purposes, we show here the impact of performing scale and charm-quark mass variations in the determination of the gluon PDF at small x . As a baseline we take the NNPDF3.0+LHCb set of Ref. [41] restricting the input data to within $p_T \in [1.0, 8.0]$ GeV to match the current analysis. This comparison is shown in Fig. 3.4. Specifically, we assess how the fit results change if the scale is varied from the default $\mu^{(\text{ref})} = \sqrt{m_c^2 + p_T^2}$ to $\mu = \sqrt{4m_c^2 + p_T^2}$ and if the charm-quark mass is varied from the default $m_c = 1.5$ GeV to 1.3 and 1.7 GeV.

From the comparison in Fig. 3.4 one observes that in all cases the results of the fits varying either the scale or the value of m_c are consistent with the baseline within uncertainties. In particular, the effects of charm-quark mass variations are much smaller than the PDF uncertainties, since they partially cancel out in the ratios in Eq. (3.1). The impact of varying $\mu^{(\text{ref})}$ is more significant and reaches the 1σ level at $x \lesssim 10^{-5}$.

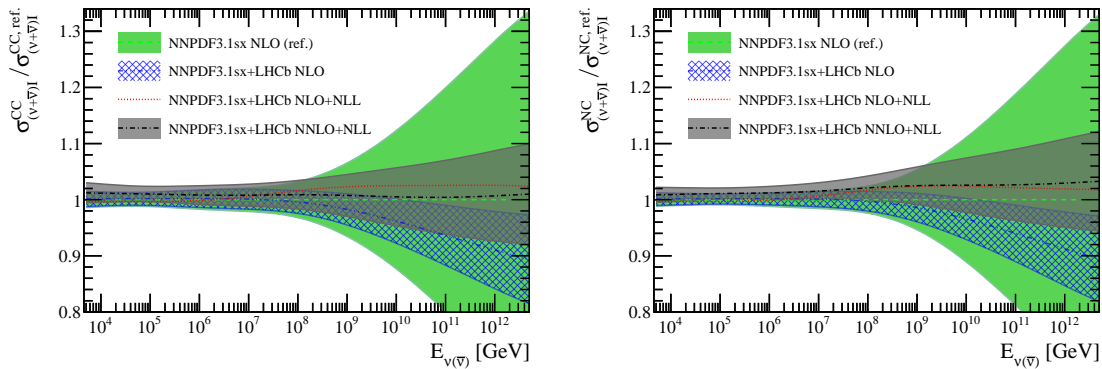


Figure 4.1. The total CC (left) and NC (right plot) neutrino-isoscalar cross-section as a function of the energy $E_{\nu(\bar{\nu})}$ for different theoretical settings. Results are shown normalised to the central value of the NNPDF3.1sx NLO calculation and averaged over neutrino- and antineutrino-induced processes. The uncertainty bands correspond to the 1σ PDF uncertainties.

4 The neutrino-nucleon cross-section at ultra-high energies

In this section we present the main results of this work, namely the predictions for the UHE (anti)neutrino-nucleon cross-section for CC and NC scattering. Firstly, the perturbative stability of our calculation is assessed by studying the convergence of results obtained with different theoretical accuracies. We then provide a comparison of our baseline predictions to previous calculations and discuss the origin of differences and similarities. Finally, we compare our predictions to recent measurements from IceCube [59] and assess the impact of nuclear corrections following the strategy outlined in Sect. 2.4.

4.1 Impact of theory settings and perturbative stability

In order to assess the perturbative stability of our calculation, we compute the total cross-section in the $n_f = 6$ FONLL scheme at NLO, NLO+NLL x , and NNLO+NLL x accuracy using the corresponding NNPDF3.1sx+LHCb PDF sets presented in Sect. 3. The results are shown in Fig. 4.1, where the total cross-section for both the CC (left) and NC (right) scattering is shown for the sum of neutrino- and antineutrino-induced processes, presented as a function of the (anti)neutrino energy $E_{\nu(\bar{\nu})}$. Predictions are normalised to the central value of those obtained with the NNPDF3.1sx NLO set (*i.e.* without the LHCb D -meson data) and the quoted uncertainties indicate the 1σ PDF uncertainty. For the NLO+NLL x predictions, we only show the central value, as the results are almost identical to those obtained at NNLO+NLL x , both in terms of central value and uncertainty. Here we assume an isoscalar target without nuclear modifications.

Fig. 4.1 reveals that the impact of the LHCb D -meson data is significant in the region $E_{\nu(\bar{\nu})} \gtrsim 10^8$ GeV. For instance, at $E_{\nu(\bar{\nu})} \simeq 10^{12}$ GeV the PDF uncertainties decrease from about 30% to below 10%. The same qualitative behaviour is observed for both CC and NC processes. A further interesting observation is that the inclusion of the LHCb D -meson data leads to a suppression of the central value of the total UHE neutrino cross-section by around 10% at the highest energies. Although this is shown here only for the NLO case, the

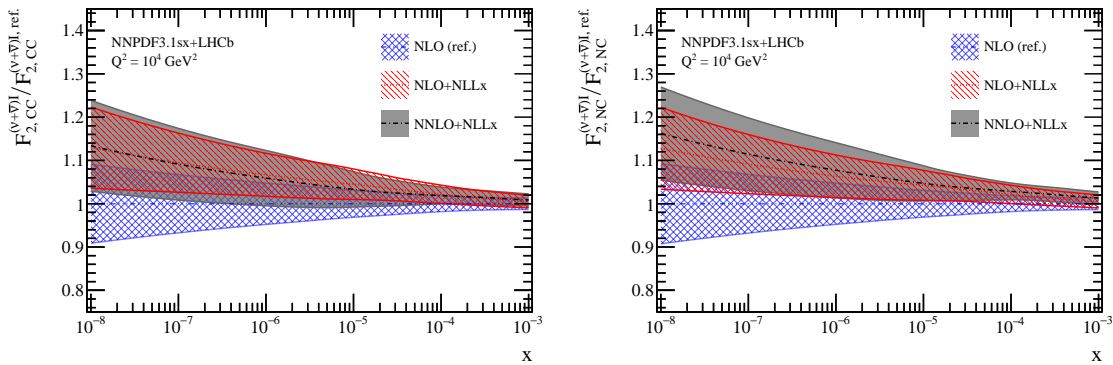


Figure 4.2. The CC (left) and NC (right plot) structure function $F_2^{\nu+\bar{\nu}}(x, Q^2)$ computed for an isoscalar target at $Q^2 = 10^4 \text{ GeV}^2$ with the NNPDF3.1sx+LHCb sets for three different theoretical settings: NLO, NLO+NLL x , and NNLO+NLL x . The structure functions are normalised to the central value the NLO calculation, with the bands indicating the 1σ PDF uncertainty.

LHCb data have a similar impact when different theory settings, such as (N)NLO+NLL x , are adopted. This is a consequence of the impact of the LHCb D -meson data on the behaviour of the gluon PDF at small x . As shown in Fig. 3.2, the LHCb data leads to relatively lower values of the gluon PDF in the small- x region (irrespective of the theory settings).

Concerning the perturbative stability, Fig. 4.1 shows that the NNPDF3.1sx+LHCb predictions are consistent within the 1σ PDF uncertainties at all considered perturbative accuracies. The central values of the NLO+NLL x and NNLO+NLL x calculations are remarkably consistent, in agreement within 1% for both CC and NC scattering across the entire range of $E_{\nu(\bar{\nu})}$ values. This difference is negligible as compared to PDFs uncertainties and nuclear corrections (see Sect. 2.4).

The perturbative stability of the UHE cross-sections upon inclusion of small- x resummation effects is a direct consequence of the stability of the structure functions. To illustrate this point, in Fig. 4.2 we show the predictions for the $F_2^{\nu+\bar{\nu}}(x, Q^2)$ structure function for both CC (left) and NC (right) scattering on an isoscalar target at $Q = 100 \text{ GeV}$, computed with the NNPDF3.1sx+LHCb sets for the three different theoretical settings: NLO, NLO+NLL x , and NNLO+NLL x . The central values of the NLO+NLL x and NNLO+NLL x structure functions differ typically by around (1-2)%, and 4% at most for NC scattering. Differences between the fixed-order and the resummed calculations are instead more pronounced and can be as large as 15% at $x \simeq 10^{-8}$. We also note that differences between the corresponding input PDF sets for each of these three theoretical settings are typically larger (see Fig. 3.2). Nonetheless, predictions for physical observables are in better agreement due to the partial compensation between PDF evolution and DIS coefficient functions.

The agreement between the NLO+NLL x and NNLO+NLL x predictions shown in Figs. 4.1 and 4.2 demonstrates the excellent convergence of the perturbative expansion at small x after resummation effects are included. This indicates that missing higher-order (MHO) corrections are likely to be small as compared to other sources of theoretical un-

certainty. Altogether, we find that the combination of the constraints from the LHCb D -meson data and the inclusion of NLL x small- x resummation leads to robust predictions for CC and NC neutrino-nucleon cross-section predictions up to the highest energies, with PDF uncertainties below 10% and negligible uncertainties due to MHO corrections. At this level of precision, other sources of theoretical uncertainty, such as nuclear corrections, cannot be neglected.

4.2 Comparison to previous calculations

As discussed in Sect. 1, predictions for the UHE neutrino-nucleus cross-sections based on a variety of the different theoretical setups have been provided in the past by a number of groups [8, 19–30]. In the following, we provide a comparison of our results (labelled as BGR18) to a number of calculations of the UHE cross-sections present in the literature. The BGR18 predictions shown here correspond to the NNLO+NLL x calculation in the $n_f = 6$ FONLL scheme with the corresponding NNPDF3.1sx+LHCb set as an input PDF set. As nuclear corrections are absent from the selected benchmark calculations, for the purpose of comparison we do not include them in our predictions.

We begin by comparing our results to the calculations from Gandhi *et al.* (GQRS98) [8], Connolly, Thorne, and Waters (CTW11) [22], and Cooper-Sarkar, Mertsch, and Sarkar (CMS11) [23], all of which have been obtained in the framework of collinear factorisation. The GQRS98 and CTW11 predictions are obtained with LO-accurate coefficient functions with CTEQ4M [92] and MSTW08 [93] PDFs respectively, while the CMS11 calculation is performed at NLO with the HERAPDF1.5 PDFs [94]. The comparison for the sum of neutrino and antineutrino cross-sections is presented in Fig. 4.3 for both the CC (left) and NC (right) processes. For GQRS98 and CTW11 we only show the central values, while for BGR18 and CMS11 we also include the PDF uncertainties. In the case of the CMS11 predictions we have added the central values of the neutrino and antineutrino induced cross-sections, and show the relative uncertainty of the neutrino induced process. The lighter and darker uncertainty bands of this prediction correspond to different prescriptions for estimating the PDF uncertainties. The darker band is obtained by excluding one particular member of the HERAPDF1.5 PDF set. This member dominates in the computation of the PDF uncertainty at small x and thus removing it results in a much smaller uncertainty band, see Ref. [23] for more details.

In general, there are marked differences between the BGR18 and the other calculations. For the case of CC scattering, we find that the BGR18 and GQRS98 predictions are in agreement in the region $10^5 \text{ GeV} \lesssim E_{\nu(\bar{\nu})} \lesssim 10^8 \text{ GeV}$, but differ significantly outside this range. At $E_{\nu(\bar{\nu})} \simeq 10^{12} \text{ GeV}$ the GQRS98 calculation is larger by around 30%, which corresponds to a deviation of more than 3σ in units of the PDF uncertainty of the BGR18 calculation. The origin of this difference can be understood by considering that the CTEQ4M PDF set used in the GQRS98 calculation must be extrapolated beyond its region of validity, $x \in [10^{-5}, 1]$. Applying the extrapolation adopted in Ref. [8], we find the CTEQ4M gluon and quark PDFs evaluated at $x \simeq 10^{-7}$ and $Q \sim 100 \text{ GeV}$ overshoot those of NNPDF3.1sx+LHCb by around 25%. While the CMS11 and CTW11 calculations are broadly consistent with one another, we find that at intermediate energies these predictions

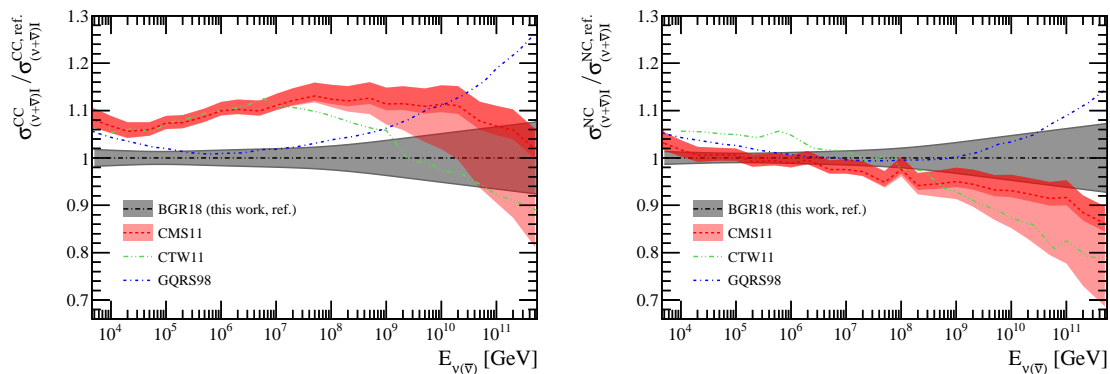


Figure 4.3. Comparison of the results of the present work (BGR18) with previous calculations of the UHE neutrino-isoscalar cross-sections as a function of $E_{\nu(\bar{\nu})}$ for CC (left) and NC (right plot) scattering, normalised to the central BGR18 value. The BGR18 predictions are provided in the $n_f = 6$ FONLL scheme at NNLO+NLL x accuracy with the corresponding NNPDF3.1sx+LHCb PDF set, and are compared to the GQRS98, CMS11, and CTW11 calculations. For both BGR18 and CMS11 the bands indicate the PDF uncertainty and in the CMS11 case the dark and light bands correspond to two alternative treatments of the PDF uncertainty, see text.

are approximately (8-10)% larger than BGR18. In the case of the CTW11 prediction, this can be partly attributed to the absence of the $\mathcal{O}(\alpha_s)$ corrections to the coefficient functions, which are negative and amount to (4-5)% for $E_{\nu(\bar{\nu})} \in [10^4, 10^8]$ GeV. The origin of the difference with respect to the CMS11 prediction (which includes these corrections) is instead likely to originate from the treatment of top-quark production. Inspection of Fig. 11 (left) of Ref. [23] suggests that the contribution to the total cross-section from b -quark initiated diagrams (top-quark production) amount to +10% at $E_\nu = 10^6$ GeV. This calculation is performed in the ZM-VFNS where heavy-quark mass effects are absent. As discussed in Sect. 2.3, our calculation of top-quark production for CC scattering includes heavy-quark mass correction to NLO. We find that at this energy the relative contribution of top-quark production is below 1% (see Fig. 2.5). At high (anti)neutrino energies, $E_{\nu(\bar{\nu})} \simeq 10^{11}$ GeV, the three calculations are instead consistent within the BGR18 uncertainties, although the CTW11 central value is suppressed by around 10% as compared to BGR18.

In the NC scattering case, the GQRS98 calculation agrees with BGR18 at intermediate values of $E_{\nu(\bar{\nu})}$ but overshoots it at higher and lower energies. The same behaviour was observed for CC scattering and these differences can again be primarily attributed to the behaviour of the input PDFs (see the discussion above). We find reasonable agreement between BGR18 and the CMS11 and CTW11 results for NC scattering. For the highest values of neutrino energies, both of these predictions tend to undershoot the BGR18 predictions. For instance, the CTW11 predictions are suppressed by around a factor 20% at $E_\nu \simeq 10^{12}$ GeV as compared to the BGR18 calculation. This can be partly traced back to differences at the level of input PDFs. However, when the PDF uncertainties of the CTW11 are accounted for (see Ref. [22]), this behaviour is not significant.

The calculations displayed in Fig. 4.3 are all based on collinear factorisation. In order to assess the sensitivity of the UHE cross-sections to other QCD theoretical frameworks, in

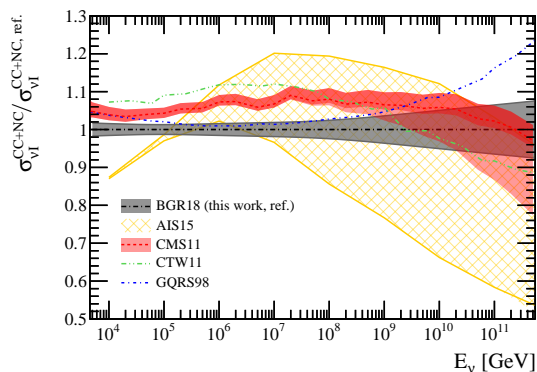


Figure 4.4. Same as Fig. (4.3), now for the sum of NC and CC neutrino-isoscalar cross-sections. In addition, the AIS15 calculation based upon the non-linear QCD (saturation) framework is included.

Fig. 4.4 we compare the total cross-section for neutrino-induced scattering (the sum of CC and NC processes) with the predictions from Albacete *et al.* (AIS15) [26]. This calculation is based on the Balitsky-Kovchegov equation with running coupling, which incorporates non-linear effects from gluon recombination (saturation).

In the AIS15 framework, the steep growth of the PDFs at small x is tamed by non-linear effects, leading to a suppression of the UHE neutrino-nucleon cross-section. Indeed, Fig. 4.4 shows that at the highest energies the AIS15 calculation is in general suppressed by about 25% as compared to the BGR18 result. However, for large neutrino energies the AIS15 prediction is affected by a large theoretical uncertainty arising from the limited information on some of the input parameters that enter the calculation. Given the small theory uncertainties of the BGR18 calculation, a possible suppression of the measured UHE cross-sections at high energies as compared to our predictions may indicate the onset of saturation effects.

4.3 Comparison to IceCube data and impact of nuclear corrections

To conclude the discussion of our results, in Fig. 4.5 we show predictions for the sum of neutrino and antineutrino scattering on different targets. We consider the case of a free isoscalar target and that of H_2O molecule, where nuclear modifications have been evaluated using the EPPS16 nPDF set (see Sect. 2.4). Results are also shown for an “isoscalar” H_2O molecule ($N \approx H_2O$), according to Eq. (2.12). These predictions are obtained from the baseline NNLO+NLL x accurate results in the $n_f = 6$ FONLL scheme and are presented as a function of E_ν for both CC (left) and NC (right) processes. The upper panels of Fig. 4.5 display the absolute cross-section, while in the lower panels the predictions are shown normalised to the central value of the BGR18 calculation on H_2O . In the CC case, we also show the recent IceCube measurements based on the 6-year HESE (high-energy showers) dataset [59]. This dataset is based on high-energy starting events (or contained-vertex events). The experimental uncertainties are the sum in quadrature of the statistical and systematic errors. Note that for the rightmost data point only a lower limit on the magnitude of the cross-section can be derived.

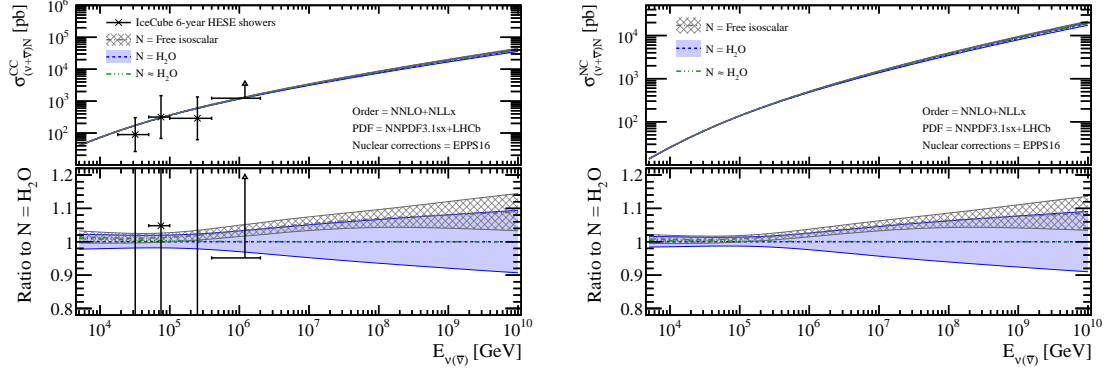


Figure 4.5. The BGR18 predictions in the $n_f = 6$ FONLL scheme at NNLO+NLL x accuracy as a function of E_ν in the CC (left) and NC (right plot) cases for two different targets: a free isoscalar nucleon (without nuclear modifications) and an H₂O target (with the EPPS16 nuclear modifications). In the lower panel, we show the same results normalised to the central value of the BGR18 calculation for an H₂O target. In the CC case, we also compare our predictions with recent IceCube measurements based on the 6-year HESE shower dataset [59].

The results in Fig. 4.5 highlight that, given the current precision of free-nucleon calculations, effects due to the nuclear modifications of the PDFs of nucleons bound inside a H₂O molecule are significant and cannot be neglected. As already discussed in Sect. 2.4, nuclear modifications induce a suppression of the UHE cross-section by up to 10% as compared to the free-nucleon case. However, uncertainties associated to these nuclear modifications are large and currently dominate over PDF and other theoretical uncertainties. The fact that nuclear modifications are now the dominant source of theoretical uncertainty on the UHE neutrino cross-section predictions provides a strong motivation to improve on the knowledge of nPDFs. This goal could be achieved by exploiting the LHC $p+Pb$ collision data as well as, in the near future, data collected at the EIC. It is worth noting that the prediction for $N \approx \text{H}_2\text{O}$ provides an excellent approximation for E_ν values. The difference between the full and approximate results at the lowest E_ν values is $\approx 1\%$.

Focussing now on the CC scattering cross-section of Fig. 4.5, we observe that the IceCube measurements extend up to neutrino energies of around $E_\nu \simeq 10^6$ GeV. At the current level of precision, these measurements cannot discriminate between the different theoretical predictions. Nonetheless, future data based on a much larger sample from neutrino telescopes, such as IceCube and KM3NET, and from other experiments sensitive to very high-energy neutrinos should improve the precision of the current measurements at intermediate energies and extend the measurement to larger E_ν values. As discussed in Sect. 4.2, the different theoretical predictions give rise to small differences at intermediate energies. The origin of these differences are well understood, and are related to the perturbative accuracy of the calculation. A cross-section measurement at higher energies would instead probe QCD in the very small- x region providing a test of the assumptions of non-perturbative information related to the distribution of quarks and gluons within bound nuclei, and may also test for the presence of saturation effects.

5 Summary and outlook

In this work, we have presented state-of-the-art predictions for the cross-sections of high-energy neutrino scattering on nucleons, with particular attention to a target material composed of H₂O molecules. With respect to previous calculations, we have made a number of major improvements.

Firstly, we have extended the calculation of deep-inelastic structure functions to NNLO matched with small- x resummation corrections at next-to-leading logarithmic (NLL x) accuracy. We find that small- x resummation corrections stabilise the perturbative convergence of the UHE neutrino cross-sections. This feature is highlighted by the similarity of the NLO+NLL x and NNLO+NLL x calculations.

The second main improvement is the inclusion of the D -meson production data from LHCb in the determination of the PDF sets used in our calculations. This dataset imposes a stringent constraint on the PDFs at small x , with a consequent significant impact on the UHE neutrino cross-section. This was achieved by producing dedicated PDF sets based on the NNPDF3.1sx sets and including the LHCb data by means of Bayesian reweighting. Due to the unavailability of small- x resummation corrections to the partonic cross-section for D -meson production, predictions for this process have instead been obtained at NLO+PS accuracy convoluted with PDFs determined including small- x resummation effects. We have demonstrated that the LHCb measurements lead to a reduction of the uncertainties on the UHE neutrino cross-sections related to PDFs by up to a factor three.

As compared to previous studies, we have introduced further improvements in our calculations. One of these is the inclusion of charm-, bottom-, and top-quark mass effects using the FONLL general-mass scheme for both CC and NC structure functions. We have also provided an estimate of the impact on the UHE cross-sections related to nuclear effects. We find that these corrections can be as large as 10% at high neutrino energies but are also affected by large uncertainties, which in turn impact the quoted precision of the calculation.

We found notable differences between our predictions and previous benchmark calculations, which can be traced back to differences in both the perturbative and non-perturbative inputs to the calculation. For example, in the energy range of $E_{\nu(\bar{\nu})} \in [6 \times 10^3, 10^5]$ GeV we find a prediction which is $\approx 5\%$ lower than the quoted SM prediction in the IceCube measurement [59]. When more precise cross-section measurements are obtained at neutrino telescopes, these effects, as well as a reliable estimate of the nuclear corrections, will eventually become relevant to interpret the data. For the moment, the recent data from IceCube are still affected by large uncertainties and do not extend to large enough energies to discriminate between the different predictions.

We foresee that our calculations could be improved in at least two ways. Firstly, we found that uncertainties attributed to nuclear effects represent one of the dominant sources of theoretical uncertainty. This uncertainty could be reduced by including in the nPDF fits measurements from the LHC in $p+Pb$ collisions to constrain the distributions in small- x region. Secondly, small- x resummation effects and NNLO corrections, once available, should also be included in the partonic cross-section for D -meson production. Our study

indicates that these corrections are likely to be small at the level of a normalised cross-section, but at the level of precision that the calculation has achieved it might be necessary to account for them.

To summarise, our analysis demonstrates how measurements of the neutrino-nucleus cross-section will represent a unique probe to test the strong interaction in an extreme regime where new dynamics are expected to arise, such as BFKL or non-linear effects. In this context, our calculations provide a robust building block for the data analysis and interpretation of neutrino telescopes in the coming years. Our results should also be relevant for other phenomenological applications, for instance to compute the attenuation of the high-energy neutrino flux as they pass through the Earth [95].

Acknowledgments

We are grateful to Aart Heijboer and Alfonso García for discussions about the KM3NET experiment, to Marco Bonvini for discussions regarding HELL, to Subir Sarkar for information about the CMS11 calculation, and to Javier Albacete and Alba Soto for providing us with the AIS15 results. We thank Hannu Paukkunen and Aleksander Kusina for providing us with the EPPS16 and nCTEQ15 Oxygen nPDF grids. We thank Rabah Abdul Khalek and Luca Rottoli for providing cross-checks relevant for some of the results presented in this paper. V. B. and J. R. are supported by an European Research Council Starting Grant ‘‘PDF4BSM’’. J. R. is also partially supported by the Netherlands Organization for Scientific Research (NWO). The research of R. G. is funded by the ERC Advanced Grant ‘‘MC@NNLO’’ (340983).

A The BGR18 UHE neutrino-nucleus cross-sections

In this appendix, we discuss the delivery of the results presented in this paper. We provide a tabulation of the total UHE cross-sections for a range of E_ν values together with the corresponding theoretical uncertainties. Results are obtained with our baseline theory settings, *i.e.* the FONLL scheme at NNLO with a maximum of $n_f = 6$ active flavours augmented by small- x resummation corrections to NLL x accuracy, and based on the NNPDF3.1sx+LHCb NNLO+NLL x PDF set.

Structure functions. In order to allow the users to reproduce our results for the double-differential cross-sections, we provide predictions for the neutrino structure functions F_2 , xF_3 , and F_L both for NC and CC scattering. Structure functions are made available in the form of interpolation grids in the LHAPDF6 format [96]. Grids for NC and CC, neutrino and antineutrino structure functions are provided for a free isoscalar target. The grids contain the $N_{\text{rep}} = 40$ Monte Carlo replicas resulting from the PDF reweighting analysis.⁷ Mean and standard deviation of a structure function F are obtained according to

$$\langle F \rangle_{\text{rep}} = \frac{1}{N_{\text{rep}}} \sum_{k=1}^{N_{\text{rep}}} F^{(k)}, \quad \delta F = \sqrt{\frac{\sum_{k=1}^{N_{\text{rep}}} (\langle F \rangle_{\text{rep}} - F^{(k)})^2}{N_{\text{rep}} - 1}}, \quad (\text{A.1})$$

⁷Note that some of the replicas are equivalent, as a consequence of the unweighting procedure [83].

where $F^{(k)}$ is the value of the structure function computed with the k -th Monte Carlo replica.

Total cross-sections. The structure function grids discussed above allow constructing the double-differential UHE neutrino cross-section with the associated PDF uncertainties. Predictions for the total cross-section can then be obtained by integrating the double-differential cross-section by means of Eq. (2.4).

While in Eq. (2.1) we presented the explicit formula for the CC cross-section, here we discuss in more detail the NC cross-section. Throughout this paper we have implicitly assumed that in our computations higher-order electroweak (EW) corrections can be neglected. However, for the computation of the NC cross-section we find advantageous to employ an “improved” scheme that includes part of the higher-order EW corrections. A pure LO treatment of the EW effects entails relations between the relevant parameters, such as G_F , M_W , M_Z and $\sin^2 \theta_W$, that lead some of them to be in strong disagreement with the measured values. In order to overcome this limitation, we employ the prescription of Ref. [97] to include in our computation the leading universal corrections, so that:

$$\frac{d^2 \sigma_{\nu(\bar{\nu})N}^{\text{NC}}(x, Q^2, E_\nu)}{dx dQ^2} = \frac{8G_F^2}{\pi x} \left[\frac{(M_Z^2 \rho - M_W^2) M_W^2}{M_Z^2 Q^2 \rho^2 (2 - \rho)} \right]^2 \times \left(Y_+ F_{2,\text{NC}}^{\nu N}(x, Q^2) \mp Y_- x F_{3,\text{NC}}^{\nu N}(x, Q^2) - y^2 F_{L,\text{NC}}^{\nu N}(x, Q^2) \right), \quad (\text{A.2})$$

where $\rho = 1 + \Delta\bar{\rho}$, with $\Delta\bar{\rho}$ given in Eq. (8.22) of Ref. [97]. Note that, in contrast with the CC case, the structure functions in Eq. (A.2) for neutrino and antineutrino scattering are the same. Therefore, the only difference between neutrino and antineutrino cross-sections is the sign of the term proportional to $x F_3$.

In addition to the free-nucleon cross-sections, we also provide the values of the nuclear correction factor $R_{\nu O}/A$ as defined in Eq. (2.10). This allows one to evaluate the central value and the associated uncertainty to the total cross-sections including the effects of nuclear modifications. Presenting the results in this format has the advantage that predictions for scattering off a molecule of H_2O can be easily updated once improved predictions for $R_{\nu O}$ become available, see Sect. 2.4. Since proton PDF uncertainties and nPDF uncertainties are uncorrelated, they can be combined by adding them in quadrature.

The BGR18 CC and NC (anti)neutrino total cross-sections, $\sigma_{\nu(\bar{\nu})I}^{\text{CC}}$ and $\sigma_{\nu(\bar{\nu})I}^{\text{NC}}$, as functions of the energy E_ν are tabulated in Tables A.1 and A.2, respectively. Results for the scattering off an isoscalar target without nuclear effects are shown along with the corresponding PDF uncertainty $\delta\sigma_{\nu(\bar{\nu})I}^{\text{CC}}$. The values for the nuclear correction factor $R_{\nu(\bar{\nu})O}/A$, Eq. (2.10), and the corresponding nPDF uncertainty $\delta R_{\nu(\bar{\nu})O}^{\text{CC}}$ are also provided.

The LHAPDF structure function grids and an example code that computes the total cross-sections tabulated in Tables A.1 and A.2 are available from the following web page:

<https://data.nnpdf.science/BGR18/>

along with a short set on instructions.

Charged-current neutrino scattering								
$E_{\nu(\bar{\nu})}$ (GeV)	$\sigma_{\nu I}^{\text{CC}}$ (pb)	$\delta\sigma_{\nu I}^{\text{CC}}$ (%)	$\frac{1}{A}R_{\nu O}^{\text{CC}}$	$\delta R_{\nu O}^{\text{CC}}$ (%)	$\sigma_{\bar{\nu} I}^{\text{CC}}$ (pb)	$\delta\sigma_{\bar{\nu} I}^{\text{CC}}$ (%)	$\frac{1}{A}R_{\bar{\nu} O}^{\text{CC}}$	$\delta R_{\bar{\nu} O}^{\text{CC}}$ (%)
5×10^3	25.5	± 2.2	1	$^{+1.2}_{-1.2}$	15.2	± 1.4	0.99	$^{+2.2}_{-2.1}$
1×10^4	44.6	± 2	1	$^{+1.2}_{-1.2}$	28.5	± 1.3	0.99	$^{+2.0}_{-1.9}$
2×10^4	73.8	± 1.8	1	$^{+1.2}_{-1.2}$	51.2	± 1.2	0.99	$^{+1.9}_{-1.8}$
5×10^4	133	± 1.5	0.99	$^{+1.3}_{-1.2}$	103	± 1.3	0.99	$^{+1.8}_{-1.6}$
1×10^5	199	± 1.4	0.99	$^{+1.5}_{-1.3}$	165	± 1.3	0.99	$^{+1.9}_{-1.6}$
2×10^5	287	± 1.4	0.98	$^{+1.8}_{-1.6}$	252	± 1.4	0.98	$^{+2.1}_{-1.8}$
5×10^5	453	± 1.5	0.97	$^{+2.5}_{-2.1}$	421	± 1.6	0.97	$^{+2.7}_{-2.3}$
1×10^6	628	± 1.6	0.97	$^{+3.1}_{-2.7}$	600	± 1.7	0.96	$^{+3.2}_{-2.9}$
2×10^6	859	± 1.8	0.96	$^{+3.7}_{-3.4}$	837	± 1.7	0.96	$^{+3.8}_{-3.5}$
5×10^6	1.28×10^3	± 1.9	0.95	$^{+4.6}_{-4.3}$	1.27×10^3	± 1.8	0.95	$^{+4.7}_{-4.3}$
1×10^7	1.71×10^3	± 2	0.94	$^{+5.3}_{-4.9}$	1.71×10^3	± 1.9	0.94	$^{+5.3}_{-5.0}$
2×10^7	2.27×10^3	± 2.1	0.94	$^{+5.9}_{-5.5}$	2.28×10^3	± 2	0.94	$^{+5.9}_{-5.5}$
5×10^7	3.26×10^3	± 2.3	0.93	$^{+6.5}_{-6.2}$	3.28×10^3	± 2.3	0.93	$^{+6.6}_{-6.3}$
1×10^8	4.25×10^3	± 2.5	0.93	$^{+7}_{-6.7}$	4.29×10^3	± 2.5	0.93	$^{+7.0}_{-6.7}$
2×10^8	5.51×10^3	± 2.8	0.92	$^{+7.4}_{-7.1}$	5.56×10^3	± 2.8	0.92	$^{+7.4}_{-7.1}$
5×10^8	7.69×10^3	± 3.3	0.92	$^{+7.9}_{-7.6}$	7.76×10^3	± 3.3	0.92	$^{+7.9}_{-7.6}$
1×10^9	9.82×10^3	± 3.7	0.92	$^{+8.2}_{-8}$	9.93×10^3	± 3.7	0.92	$^{+8.2}_{-8.0}$
2×10^9	1.25×10^4	± 4.1	0.91	$^{+8.5}_{-8.3}$	1.26×10^4	± 4.1	0.91	$^{+8.5}_{-8.3}$
5×10^9	1.7×10^4	± 4.7	0.91	$^{+8.8}_{-8.6}$	1.72×10^4	± 4.7	0.91	$^{+8.8}_{-8.6}$
1×10^{10}	2.14×10^4	± 5.1	0.91	$^{+9}_{-8.8}$	2.17×10^4	± 5.1	0.91	$^{+9.0}_{-8.8}$
2×10^{10}	2.69×10^4	± 5.6	0.91	$^{+9.2}_{-9}$	2.72×10^4	± 5.6	0.91	$^{+9.2}_{-9.0}$
5×10^{10}	3.6×10^4	± 6.1	0.9	$^{+9.4}_{-9.3}$	3.64×10^4	± 6.1	0.9	$^{+9.4}_{-9.3}$
1×10^{11}	4.47×10^4	± 6.6	0.9	$^{+9.5}_{-9.4}$	4.52×10^4	± 6.6	0.9	$^{+9.5}_{-9.4}$
2×10^{11}	5.54×10^4	± 7	0.9	$^{+9.6}_{-9.5}$	5.61×10^4	± 7	0.9	$^{+9.6}_{-9.5}$
5×10^{11}	7.32×10^4	± 7.6	0.9	$^{+9.7}_{-9.6}$	7.41×10^4	± 7.6	0.9	$^{+9.7}_{-9.6}$
1×10^{12}	9×10^4	± 8	0.9	$^{+9.8}_{-9.7}$	9.12×10^4	± 8	0.9	$^{+9.8}_{-9.7}$
2×10^{12}	1.1×10^5	± 8.4	0.9	$^{+9.8}_{-9.7}$	1.12×10^5	± 8.4	0.9	$^{+9.8}_{-9.7}$
5×10^{12}	1.44×10^5	± 8.9	0.9	$^{+9.9}_{-9.8}$	1.45×10^5	± 8.9	0.9	$^{+9.9}_{-9.8}$

Table A.1. The BGR18 charged-current neutrino total cross-sections $\sigma_{\nu(\bar{\nu})I}^{\text{CC}}$ as a function of the energy E_{ν} . We show the results for the scattering of a (anti)neutrino off a free isoscalar target together with the percentage proton PDF uncertainties, $\delta\sigma_{\nu(\bar{\nu})I}^{\text{CC}}$. We also list the values of the nuclear correction factor $R_{\nu(\bar{\nu})O}/A$, Eq. (2.10), computed with the EPPS16 set and the percentage nPDF uncertainty, $\delta R_{\nu(\bar{\nu})O}^{\text{CC}}$.

Neutral-current neutrino scattering								
$E_{\nu(\bar{\nu})}$ (GeV)	$\sigma_{\nu I}^{\text{NC}}$ (pb)	$\delta\sigma_{\nu I}^{\text{NC}}$ (%)	$\frac{1}{A}R_{\nu O}^{\text{NC}}$	$\delta R_{\nu O}^{\text{NC}}$ (%)	$\sigma_{\bar{\nu} I}^{\text{NC}}$ (pb)	$\delta\sigma_{\bar{\nu} I}^{\text{NC}}$ (%)	$\frac{1}{A}R_{\bar{\nu} O}^{\text{NC}}$	$\delta R_{\bar{\nu} O}^{\text{NC}}$ (%)
5×10^3	8.45	± 1.7	1	$^{+0.83}_{-0.84}$	5.52	± 0.96	0.99	$^{+1.4}_{-1.3}$
1×10^4	15.1	± 1.5	1	$^{+0.81}_{-0.82}$	10.4	± 0.91	0.99	$^{+1.3}_{-1.3}$
2×10^4	25.8	± 1.4	1	$^{+0.81}_{-0.79}$	19	± 0.89	0.99	$^{+1.2}_{-1.2}$
5×10^4	48.6	± 1.1	1	$^{+0.88}_{-0.79}$	38.9	± 0.9	0.99	$^{+1.2}_{-1.1}$
1×10^5	74.6	± 1	0.99	$^{+1}_{-0.89}$	63.5	± 0.94	0.99	$^{+1.3}_{-1.1}$
2×10^5	111	± 0.96	0.99	$^{+1.3}_{-1.1}$	99.5	± 0.99	0.99	$^{+1.5}_{-1.3}$
5×10^5	182	± 1	0.98	$^{+2}_{-1.7}$	170	± 1.1	0.98	$^{+2.1}_{-1.9}$
1×10^6	258	± 1.1	0.97	$^{+2.6}_{-2.3}$	248	± 1.2	0.97	$^{+2.7}_{-2.4}$
2×10^6	361	± 1.2	0.97	$^{+3.3}_{-3}$	352	± 1.2	0.96	$^{+3.4}_{-3.1}$
5×10^6	552	± 1.3	0.96	$^{+4.2}_{-3.9}$	545	± 1.3	0.96	$^{+4.3}_{-4.0}$
1×10^7	751	± 1.4	0.95	$^{+4.9}_{-4.6}$	746	± 1.4	0.95	$^{+4.9}_{-4.6}$
2×10^7	1.01×10^3	± 1.6	0.94	$^{+5.5}_{-5.2}$	1.01×10^3	± 1.6	0.94	$^{+5.5}_{-5.2}$
5×10^7	1.48×10^3	± 1.8	0.94	$^{+6.2}_{-6}$	1.47×10^3	± 1.8	0.94	$^{+6.3}_{-6.0}$
1×10^8	1.95×10^3	± 2	0.93	$^{+6.7}_{-6.5}$	1.95×10^3	± 2	0.93	$^{+6.7}_{-6.5}$
2×10^8	2.55×10^3	± 2.3	0.93	$^{+7.2}_{-6.9}$	2.55×10^3	± 2.3	0.93	$^{+7.2}_{-6.9}$
5×10^8	3.6×10^3	± 2.8	0.92	$^{+7.6}_{-7.4}$	3.6×10^3	± 2.8	0.92	$^{+7.7}_{-7.4}$
1×10^9	4.63×10^3	± 3.2	0.92	$^{+8}_{-7.8}$	4.63×10^3	± 3.2	0.92	$^{+8.0}_{-7.8}$
2×10^9	5.93×10^3	± 3.7	0.92	$^{+8.3}_{-8.1}$	5.93×10^3	± 3.7	0.92	$^{+8.3}_{-8.1}$
5×10^9	8.15×10^3	± 4.3	0.91	$^{+8.6}_{-8.5}$	8.15×10^3	± 4.3	0.91	$^{+8.6}_{-8.5}$
1×10^{10}	1.03×10^4	± 4.7	0.91	$^{+8.9}_{-8.7}$	1.03×10^4	± 4.7	0.91	$^{+8.9}_{-8.7}$
2×10^{10}	1.3×10^4	± 5.2	0.91	$^{+9.1}_{-8.9}$	1.3×10^4	± 5.2	0.91	$^{+9.1}_{-8.9}$
5×10^{10}	1.75×10^4	± 5.7	0.91	$^{+9.3}_{-9.2}$	1.75×10^4	± 5.7	0.91	$^{+9.3}_{-9.2}$
1×10^{11}	2.18×10^4	± 6.2	0.91	$^{+9.4}_{-9.3}$	2.18×10^4	± 6.2	0.91	$^{+9.4}_{-9.3}$
2×10^{11}	2.71×10^4	± 6.6	0.9	$^{+9.6}_{-9.5}$	2.71×10^4	± 6.6	0.9	$^{+9.6}_{-9.5}$
5×10^{11}	3.6×10^4	± 7.2	0.9	$^{+9.7}_{-9.6}$	3.6×10^4	± 7.2	0.9	$^{+9.7}_{-9.6}$
1×10^{12}	4.44×10^4	± 7.6	0.9	$^{+9.7}_{-9.6}$	4.44×10^4	± 7.6	0.9	$^{+9.7}_{-9.6}$
2×10^{12}	5.46×10^4	± 8.1	0.9	$^{+9.8}_{-9.7}$	5.46×10^4	± 8.1	0.9	$^{+9.8}_{-9.7}$
5×10^{12}	7.14×10^4	± 8.6	0.9	$^{+9.8}_{-9.7}$	7.14×10^4	± 8.6	0.9	$^{+9.8}_{-9.7}$

Table A.2. Same as Table A.1 for the neutral-current scattering cross-sections.

References

- [1] T. K. Gaisser, F. Halzen, and T. Stanev, *Particle astrophysics with high-energy neutrinos*, *Phys. Rept.* **258** (1995) 173–236, [[hep-ph/9410384](#)]. [Erratum: *Phys. Rept.*271,355(1996)].
- [2] F. Halzen and S. R. Klein, *IceCube: An Instrument for Neutrino Astronomy*, *Rev. Sci. Instrum.* **81** (2010) 081101, [[arXiv:1007.1247](#)].
- [3] F. Halzen and D. Hooper, *High-energy neutrino astronomy: The Cosmic ray connection*, *Rept. Prog. Phys.* **65** (2002) 1025–1078, [[astro-ph/0204527](#)].
- [4] **IceCube** Collaboration, *Neutrino emission from the direction of the blazar TXS 0506+056 prior to the IceCube-170922A alert*, *Science* **361** (2018), no. 6398 147–151.
- [5] L. A. Anchordoqui et al., *Cosmic Neutrino Pevatrons: A Brand New Pathway to Astronomy, Astrophysics, and Particle Physics*, *JHEAp* **1-2** (2014) 1–30, [[arXiv:1312.6587](#)].
- [6] K. Murase, R. Laha, S. Ando, and M. Ahlers, *Testing the Dark Matter Scenario for PeV Neutrinos Observed in IceCube*, *Phys. Rev. Lett.* **115** (2015), no. 7 071301, [[arXiv:1503.04663](#)].
- [7] J. Salvado, O. Mena, S. Palomares-Ruiz, and N. Rius, *Non-standard interactions with high-energy atmospheric neutrinos at IceCube*, *JHEP* **01** (2017) 141, [[arXiv:1609.03450](#)].
- [8] R. Gandhi, C. Quigg, M. H. Reno, and I. Sarcevic, *Neutrino interactions at ultrahigh-energies*, *Phys. Rev.* **D58** (1998) 093009, [[hep-ph/9807264](#)].
- [9] **IceCube** Collaboration, M. Aartsen et al., *Observation of High-Energy Astrophysical Neutrinos in Three Years of IceCube Data*, *Phys.Rev.Lett.* **113** (2014) 101101, [[arXiv:1405.5303](#)].
- [10] **IceCube** Collaboration, A. Achterberg et al., *First Year Performance of The IceCube Neutrino Telescope*, *Astropart. Phys.* **26** (2006) 155–173, [[astro-ph/0604450](#)].
- [11] **KM3Net** Collaboration, S. Adrian-Martinez et al., *Letter of intent for KM3NeT 2.0*, *J. Phys.* **G43** (2016), no. 8 084001, [[arXiv:1601.07459](#)].
- [12] **BAIKAL** Collaboration, I. A. Belolaptikov et al., *The Baikal underwater neutrino telescope: Design, performance and first results*, *Astropart. Phys.* **7** (1997) 263–282.
- [13] **GRAND** Collaboration, O. Martineau-Huynh et al., *The Giant Radio Array for Neutrino Detection*, *EPJ Web Conf.* **135** (2017) 02001, [[arXiv:1702.01395](#)].
- [14] **ANITA** Collaboration, P. W. Gorham et al., *Observational Constraints on the Ultra-high Energy Cosmic Neutrino Flux from the Second Flight of the ANITA Experiment*, *Phys. Rev.* **D82** (2010) 022004, [[arXiv:1003.2961](#)]. [Erratum: *Phys. Rev.*D85,049901(2012)].
- [15] J. Rojo et al., *The PDF4LHC report on PDFs and LHC data: Results from Run I and preparation for Run II*, *J. Phys.* **G42** (2015) 103103, [[arXiv:1507.00556](#)].
- [16] J. Gao, L. Harland-Lang, and J. Rojo, *The Structure of the Proton in the LHC Precision Era*, *Phys. Rept.* **742** (2018) 1–121, [[arXiv:1709.04922](#)].
- [17] S. Forte, E. Laenen, P. Nason, and J. Rojo, *Heavy quarks in deep-inelastic scattering*, *Nucl. Phys.* **B834** (2010) 116–162, [[arXiv:1001.2312](#)].
- [18] G. Altarelli, R. D. Ball, and S. Forte, *Small x Resummation with Quarks: Deep-Inelastic Scattering*, *Nucl. Phys.* **B799** (2008) 199–240, [[arXiv:0802.0032](#)].

- [19] M. Gluck, S. Kretzer, and E. Reya, *Dynamical QCD predictions for ultrahigh-energy neutrino cross-sections*, *Astropart. Phys.* **11** (1999) 327–334, [[astro-ph/9809273](#)].
- [20] A. Cooper-Sarkar and S. Sarkar, *Predictions for high energy neutrino cross-sections from the ZEUS global PDF fits*, *JHEP* **01** (2008) 075, [[arXiv:0710.5303](#)].
- [21] R. Gandhi, C. Quigg, M. H. Reno, and I. Sarcevic, *Ultrahigh-energy neutrino interactions*, *Astropart. Phys.* **5** (1996) 81–110, [[hep-ph/9512364](#)].
- [22] A. Connolly, R. S. Thorne, and D. Waters, *Calculation of High Energy Neutrino-Nucleon Cross Sections and Uncertainties Using the MSTW Parton Distribution Functions and Implications for Future Experiments*, *Phys. Rev.* **D83** (2011) 113009, [[arXiv:1102.0691](#)].
- [23] A. Cooper-Sarkar, P. Mertsch, and S. Sarkar, *The high energy neutrino cross-section in the Standard Model and its uncertainty*, *JHEP* **08** (2011) 042, [[arXiv:1106.3723](#)].
- [24] D. A. Dicus, S. Kretzer, W. W. Repko, and C. Schmidt, *Ultrahigh-energy neutrino nucleon cross-sections and perturbative unitarity*, *Phys. Lett.* **B514** (2001) 103–108, [[hep-ph/0103207](#)].
- [25] R. Fiore, L. L. Jenkovszky, A. V. Kotikov, F. Paccanoni, and A. Papa, *Asymptotic neutrino-nucleon cross section and saturation effects*, *Phys. Rev.* **D73** (2006) 053012, [[hep-ph/0512259](#)].
- [26] J. L. Albacete, J. I. Illana, and A. Soto-Ontoso, *Neutrino-nucleon cross section at ultrahigh energy and its astrophysical implications*, *Phys. Rev.* **D92** (2015), no. 1 014027, [[arXiv:1505.06583](#)].
- [27] V. P. Goncalves and D. R. Gratieri, *Investigating the effects of the QCD dynamics in the neutrino absorption by the Earth’s interior at ultrahigh energies*, *Phys. Rev.* **D92** (2015), no. 11 113007, [[arXiv:1510.03186](#)].
- [28] C. A. Argüelles, F. Halzen, L. Wille, M. Kroll, and M. H. Reno, *High-energy behavior of photon, neutrino, and proton cross sections*, *Phys. Rev.* **D92** (2015), no. 7 074040, [[arXiv:1504.06639](#)].
- [29] M. M. Block, L. Durand, P. Ha, and D. W. McKay, *Implications of a Froissart bound saturation of $\gamma^* + p$ deep inelastic scattering. II. Ultrahigh energy neutrino interactions*, *Phys. Rev.* **D88** (2013), no. 1 013003, [[arXiv:1302.6127](#)].
- [30] J. Jalilian-Marian, *Enhancement and suppression of the neutrino nucleon total cross-section at ultrahigh-energies*, *Phys. Rev.* **D68** (2003) 054005, [[hep-ph/0301238](#)]. [Erratum: *Phys. Rev.* **D70**, 079903(2004)].
- [31] M. Bonvini, S. Marzani, and T. Peraro, *Small- x resummation from HELL*, *Eur. Phys. J.* **C76** (2016), no. 11 597, [[arXiv:1607.02153](#)].
- [32] M. Bonvini, S. Marzani, and C. Muselli, *Towards parton distribution functions with small- x resummation: HELL 2.0*, *JHEP* **12** (2017) 117, [[arXiv:1708.07510](#)].
- [33] R. D. Ball, V. Bertone, M. Bonvini, S. Forte, P. Groth Merrild, J. Rojo, and L. Rottoli, *Intrinsic charm in a matched general-mass scheme*, *Phys. Lett.* **B754** (2016) 49–58, [[arXiv:1510.00009](#)].
- [34] R. D. Ball, V. Bertone, M. Bonvini, S. Marzani, J. Rojo, and L. Rottoli, *Parton distributions with small- x resummation: evidence for BFKL dynamics in HERA data*, *Eur. Phys. J.* **C78** (2018), no. 4 321, [[arXiv:1710.05935](#)].

- [35] **xFitter Developers' Team** Collaboration, H. Abdolmaleki et al., *Impact of low- x resummation on QCD analysis of HERA data*, [arXiv:1802.00064](#).
- [36] F. Caola, S. Forte, and J. Rojo, *Deviations from NLO QCD evolution in inclusive HERA data*, *Phys. Lett.* **B686** (2010) 127–135, [[arXiv:0910.3143](#)].
- [37] F. Caola, S. Forte, and J. Rojo, *HERA data and DGLAP evolution: Theory and phenomenology*, *Nucl.Phys.* **A854** (2011) 32–44, [[arXiv:1007.5405](#)].
- [38] **LHCb** Collaboration, R. Aaij et al., *Measurements of prompt charm production cross-sections in pp collisions at $\sqrt{s} = 5$ TeV*, *JHEP* **06** (2017) 147, [[arXiv:1610.02230](#)].
- [39] **LHCb** Collaboration, R. Aaij et al., *Measurements of prompt charm production cross-sections in pp collisions at $\sqrt{s} = 13$ TeV*, *JHEP* **03** (2016) 159, [[arXiv:1510.01707](#)]. [Erratum: *JHEP*09,013(2016)].
- [40] **LHCb** Collaboration, R. Aaij et al., *Prompt charm production in pp collisions at $\sqrt{s}=7$ TeV*, *Nucl.Phys.* **B871** (2013) 1–20, [[arXiv:1302.2864](#)].
- [41] R. Gauld and J. Rojo, *Precision determination of the small- x gluon from charm production at LHCb*, *Phys. Rev. Lett.* **118** (2017), no. 7 072001, [[arXiv:1610.09373](#)].
- [42] **PROSA** Collaboration, O. Zenaiev et al., *Impact of heavy-flavour production cross sections measured by the LHCb experiment on parton distribution functions at low x* , *Eur. Phys. J.* **C75** (2015), no. 8 396, [[arXiv:1503.04581](#)].
- [43] R. Gauld, J. Rojo, L. Rottoli, and J. Talbert, *Charm production in the forward region: constraints on the small- x gluon and backgrounds for neutrino astronomy*, *JHEP* **11** (2015) 009, [[arXiv:1506.08025](#)].
- [44] M. Cacciari, M. L. Mangano, and P. Nason, *Gluon PDF constraints from the ratio of forward heavy-quark production at the LHC at $\sqrt{S} = 7$ and 13 TeV*, *Eur. Phys. J.* **C75** (2015), no. 12 610, [[arXiv:1507.06197](#)].
- [45] R. Enberg, M. H. Reno, and I. Sarcevic, *Prompt neutrino fluxes from atmospheric charm*, *Phys.Rev.* **D78** (2008) 043005, [[arXiv:0806.0418](#)].
- [46] R. Gauld, J. Rojo, L. Rottoli, S. Sarkar, and J. Talbert, *The prompt atmospheric neutrino flux in the light of LHCb*, *JHEP* **02** (2016) 130, [[arXiv:1511.06346](#)].
- [47] **PROSA** Collaboration, M. V. Garzelli, S. Moch, O. Zenaiev, A. Cooper-Sarkar, A. Geiser, K. Lipka, R. Placakyte, and G. Sigl, *Prompt neutrino fluxes in the atmosphere with PROSA parton distribution functions*, *JHEP* **05** (2017) 004, [[arXiv:1611.03815](#)].
- [48] G. Gelmini, P. Gondolo, and G. Varieschi, *Prompt atmospheric neutrinos and muons: NLO versus LO QCD predictions*, *Phys.Rev.* **D61** (2000) 036005, [[hep-ph/9904457](#)].
- [49] A. Martin, M. Ryskin, and A. Stasto, *Prompt neutrinos from atmospheric $c\bar{c}$ and $b\bar{b}$ production and the gluon at very small x* , *Acta Phys.Polon.* **B34** (2003) 3273–3304, [[hep-ph/0302140](#)].
- [50] A. Bhattacharya, R. Enberg, M. H. Reno, I. Sarcevic, and A. Stasto, *Perturbative charm production and the prompt atmospheric neutrino flux in light of RHIC and LHC*, *JHEP* **06** (2015) 110, [[arXiv:1502.01076](#)].
- [51] A. Bhattacharya, R. Enberg, Y. S. Jeong, C. S. Kim, M. H. Reno, I. Sarcevic, and A. Stasto, *Prompt atmospheric neutrino fluxes: perturbative QCD models and nuclear effects*, *JHEP* **11** (2016) 167, [[arXiv:1607.00193](#)].

- [52] M. Benzke, M. V. Garzelli, B. Kniehl, G. Kramer, S. Moch, and G. Sigl, *Prompt neutrinos from atmospheric charm in the general-mass variable-flavor-number scheme*, *JHEP* **12** (2017) 021, [[arXiv:1705.10386](#)].
- [53] F. Halzen and L. Wille, *Charm contribution to the atmospheric neutrino flux*, *Phys. Rev.* **D94** (2016), no. 1 014014, [[arXiv:1605.01409](#)].
- [54] M. V. Garzelli, S. Moch, and G. Sigl, *Lepton fluxes from atmospheric charm revisited*, *JHEP* **10** (2015) 115, [[arXiv:1507.01570](#)].
- [55] D. de Florian, R. Sassot, P. Zurita, and M. Stratmann, *Global Analysis of Nuclear Parton Distributions*, *Phys.Rev.* **D85** (2012) 074028, [[arXiv:1112.6324](#)].
- [56] K. J. Eskola, P. Paakkinen, H. Paukkunen, and C. A. Salgado, *EPPS16: Nuclear parton distributions with LHC data*, *Eur. Phys. J.* **C77** (2017), no. 3 163, [[arXiv:1612.05741](#)].
- [57] K. Kovarik et al., *nCTEQ15 - Global analysis of nuclear parton distributions with uncertainties in the CTEQ framework*, *Phys. Rev.* **D93** (2016), no. 8 085037, [[arXiv:1509.00792](#)].
- [58] H. Khanpour and S. Atashbar Tehrani, *Global Analysis of Nuclear Parton Distribution Functions and Their Uncertainties at Next-to-Next-to-Leading Order*, *Phys. Rev.* **D93** (2016), no. 1 014026, [[arXiv:1601.00939](#)].
- [59] **IceCube** Collaboration, M. G. Aartsen et al., *Measurement of the multi-TeV neutrino cross section with IceCube using Earth absorption*, *Nature* **551** (2017) 596–600, [[arXiv:1711.08119](#)].
- [60] M. Bustamante and A. Connolly, *Measurement of the Energy-Dependent Neutrino-Nucleon Cross Section Above 10 TeV Using IceCube Showers*, [arXiv:1711.11043](#).
- [61] M. Bonvini, *Small- x phenomenology at the LHC and beyond: HELL 3.0 and the case of the Higgs cross section*, [arXiv:1805.08785](#).
- [62] V. Bertone, S. Carrazza, and J. Rojo, *APFEL: A PDF Evolution Library with QED corrections*, *Comput.Phys.Commun.* **185** (2014) 1647–1668, [[arXiv:1310.1394](#)].
- [63] E. L. Berger, J. Gao, C. S. Li, Z. L. Liu, and H. X. Zhu, *Charm-Quark Production in Deep-Inelastic Neutrino Scattering at Next-to-Next-to-Leading Order in QCD*, *Phys. Rev. Lett.* **116** (2016), no. 21 212002, [[arXiv:1601.05430](#)].
- [64] J. Gao, *Massive charged-current coefficient functions in deep-inelastic scattering at NNLO and impact on strange-quark distributions*, *JHEP* **02** (2018) 026, [[arXiv:1710.04258](#)].
- [65] **NNPDF** Collaboration, R. D. Ball et al., *Impact of Heavy Quark Masses on Parton Distributions and LHC Phenomenology*, *Nucl. Phys.* **B849** (2011) 296–363, [[arXiv:1101.1300](#)].
- [66] T. Hahn, *CUBA: A Library for multidimensional numerical integration*, *Comput. Phys. Commun.* **168** (2005) 78–95, [[hep-ph/0404043](#)].
- [67] J. A. Formaggio and G. P. Zeller, *From eV to EeV: Neutrino Cross Sections Across Energy Scales*, *Rev. Mod. Phys.* **84** (2012) 1307–1341, [[arXiv:1305.7513](#)].
- [68] **The NNPDF** Collaboration, L. Del Debbio, S. Forte, J. I. Latorre, A. Piccione, and J. Rojo, *Unbiased determination of the proton structure function $f_2(p)$ with estimation*, *JHEP* **03** (2005) 080, [[hep-ph/0501067](#)].

- [69] V. Barger, E. Basso, Y. Gao, and W.-Y. Keung, *Neutrino signals in IceCube from weak production of top and charm quarks*, *Phys. Rev.* **D95** (2017), no. 9 093002, [[arXiv:1611.00773](#)].
- [70] **The xFitter Developers Team** Collaboration, V. Bertone et al., *Impact of the heavy quark matching scales in PDF fits*, *Eur. Phys. J.* **C77** (2017), no. 12 837, [[arXiv:1707.05343](#)].
- [71] L. Frankfurt, V. Guzey, and M. Strikman, *Leading Twist Nuclear Shadowing Phenomena in Hard Processes with Nuclei*, *Phys. Rept.* **512** (2012) 255–393, [[arXiv:1106.2091](#)].
- [72] S. Dulat, T.-J. Hou, J. Gao, M. Guzzi, J. Huston, P. Nadolsky, J. Pumplin, C. Schmidt, D. Stump, and C. P. Yuan, *New parton distribution functions from a global analysis of quantum chromodynamics*, *Phys. Rev.* **D93** (2016), no. 3 033006, [[arXiv:1506.07443](#)].
- [73] **LHCb** Collaboration, R. Aaij et al., *Study of prompt D^0 meson production in pPb collisions at $\sqrt{s_{NN}} = 5$ TeV*, *JHEP* **10** (2017) 090, [[arXiv:1707.02750](#)].
- [74] A. Kusina, J.-P. Lansberg, I. Schienbein, and H.-S. Shao, *Gluon shadowing and antishadowing in heavy-flavor production at the LHC*, [[arXiv:1712.07024](#)].
- [75] D. Boer, M. Diehl, R. Milner, R. Venugopalan, W. Vogelsang, et al., *Gluons and the quark sea at high energies: Distributions, polarization, tomography*, [[arXiv:1108.1713](#)].
- [76] **LHeC Study Group** Collaboration, J. Abelleira Fernandez et al., *A Large Hadron Electron Collider at CERN: Report on the Physics and Design Concepts for Machine and Detector*, *J.Phys.* **G39** (2012) 075001, [[arXiv:1206.2913](#)].
- [77] **NNPDF** Collaboration, R. D. Ball et al., *Parton distributions from high-precision collider data*, *Eur. Phys. J.* **C77** (2017), no. 10 663, [[arXiv:1706.00428](#)].
- [78] **ZEUS, H1** Collaboration, H. Abramowicz et al., *Combination of measurements of inclusive deep inelastic $e^\pm p$ scattering cross sections and QCD analysis of HERA data*, *Eur. Phys. J.* **C75** (2015), no. 12 580, [[arXiv:1506.06042](#)].
- [79] A. Guffanti and J. Rojo, *Top production at the LHC: the impact of PDF uncertainties and correlations*, [[arXiv:1008.4671](#)].
- [80] M. Czakon, D. Heymes, and A. Mitov, *High-precision differential predictions for top-quark pairs at the LHC*, *Phys. Rev. Lett.* **116** (2016), no. 8 082003, [[arXiv:1511.00549](#)].
- [81] R. Ball and R. K. Ellis, *Heavy quark production at high-energy*, *JHEP* **0105** (2001) 053, [[hep-ph/0101199](#)].
- [82] **The NNPDF** Collaboration, R. D. Ball et al., *Reweighting NNPDFs: the W lepton asymmetry*, *Nucl. Phys.* **B849** (2011) 112–143, [[arXiv:1012.0836](#)].
- [83] R. D. Ball, V. Bertone, F. Cerutti, L. Del Debbio, S. Forte, et al., *Reweighting and Unweighting of Parton Distributions and the LHC W lepton asymmetry data*, *Nucl.Phys.* **B855** (2012) 608–638, [[arXiv:1108.1758](#)].
- [84] P. Nason, S. Dawson, and R. K. Ellis, *The Total Cross-Section for the Production of Heavy Quarks in Hadronic Collisions*, *Nucl.Phys.* **B303** (1988) 607.
- [85] P. Nason, *A New method for combining NLO QCD with shower Monte Carlo algorithms*, *JHEP* **0411** (2004) 040, [[hep-ph/0409146](#)].
- [86] S. Frixione, P. Nason, and C. Oleari, *Matching NLO QCD computations with Parton Shower simulations: the POWHEG method*, *JHEP* **0711** (2007) 070, [[arXiv:0709.2092](#)].

- [87] S. Alioli, P. Nason, C. Oleari, and E. Re, *A general framework for implementing NLO calculations in shower Monte Carlo programs: the POWHEG BOX*, *JHEP* **1006** (2010) 043, [[arXiv:1002.2581](#)].
- [88] S. Frixione, P. Nason, and G. Ridolfi, *A Positive-weight next-to-leading-order Monte Carlo for heavy flavour hadroproduction*, *JHEP* **0709** (2007) 126, [[arXiv:0707.3088](#)].
- [89] T. Sjostrand, S. Mrenna, and P. Z. Skands, *A Brief Introduction to PYTHIA 8.1*, *Comput. Phys. Commun.* **178** (2008) 852–867, [[arXiv:0710.3820](#)].
- [90] T. Sjöstrand, S. Ask, J. R. Christiansen, R. Corke, N. Desai, et al., *An Introduction to PYTHIA 8.2*, *Comput.Phys.Commun.* **191** (2015) 159–177, [[arXiv:1410.3012](#)].
- [91] P. Skands, S. Carrazza, and J. Rojo, *Tuning PYTHIA 8.1: the Monash 2013 Tune*, *European Physical Journal* **74** (2014) 3024, [[arXiv:1404.5630](#)].
- [92] H. L. Lai, J. Huston, S. Kuhlmann, F. I. Olness, J. F. Owens, D. E. Soper, W. K. Tung, and H. Weerts, *Improved parton distributions from global analysis of recent deep inelastic scattering and inclusive jet data*, *Phys. Rev.* **D55** (1997) 1280–1296, [[hep-ph/9606399](#)].
- [93] A. D. Martin, W. J. Stirling, R. S. Thorne, and G. Watt, *Parton distributions for the LHC*, *Eur. Phys. J.* **C63** (2009) 189–285, [[arXiv:0901.0002](#)].
- [94] **ZEUS, H1** Collaboration, A. Cooper-Sarkar, *Proton Structure from HERA to LHC*, in *Proceedings, 40th International Symposium on Multiparticle Dynamics (ISMD 2010): Antwerp, Belgium, September 21-25, 2010*, 2010. [arXiv:1012.1438](#).
- [95] A. C. Vincent, C. A. Argüelles, and A. Kheirandish, *High-energy neutrino attenuation in the Earth and its associated uncertainties*, *JCAP* **1711** (2017), no. 11 012, [[arXiv:1706.09895](#)]. [[JCAP1711,012\(2017\)](#)].
- [96] A. Buckley, J. Ferrando, S. Lloyd, K. Nordström, B. Page, et al., *LHAPDF6: parton density access in the LHC precision era*, *Eur.Phys.J.* **C75** (2015), no. 3 132, [[arXiv:1412.7420](#)].
- [97] A. Denner, *Techniques for calculation of electroweak radiative corrections at the one loop level and results for W physics at LEP-200*, *Fortsch. Phys.* **41** (1993) 307–420, [[arXiv:0709.1075](#)].